Master RADMEP

Master Radiation and Its Effects on Microelectronics and PhotonicsTechnologies (RADMEP)

Dosimetry Study in an X-ray Irradiator: Monte Carlo Simulations and Experimental Results on Radio-Photoluminescence Samples

Master Thesis Report

Presented By

Abrham Kassa Alem

and defended at

University of Jean Monnet

23-08-2023

Host Supervisor: Prof. Matteo Ferrari
Academic Supervisor: Prof. Sylvain Girard

Jury Committee :

Prof. Sylvain Girard, University of Jean Monnet
Prof. Frederic Saigne, University of Montpellier
Prof. dr. ir. Paul Leroux, Ku Leuven University
Prof. Arto Javanainen, Jyvaskyla University

Erasmus+

Dosimetry Study in an X-ray Irradiator: Monte Carlo Simulations and Experimental Results on Radio-Photoluminescence Samples

By

Abrham Kassa Alem

A master's thesis submitted to European Joint Master's Degree in Radiation and Its Effects on Microelectronics and Photonics Technologies program in partial fulfilment of the requirements for a master of science degree.

August 23, 2023

Abstract

Matter's exposure to ionizing radiations leads to a variety of possible interactions. Depending on the specific interaction type, energy can be deposited into matter via different mechanisms. The quantification of the absorbed dose in matter is crucial to monitor the radiation levels and asses radiation effects in matter in different application areas such as radiation therapy, particle accelerators, space applications, and high-energy nuclear radiation facilities. The stochastic nature of radiation-matter interaction often requires the use of Monte Carlo tools in dosimetry applications. In the present work, a commercial X-ray irradiator is modeled using PHITS general Monte Carlo tool, aiming at verifying the possibility of using it for the irradiation of various types of macroscopic samples at high doses, ranging between the kGy and the MGy levels. Simulated particle fluence spectra evidence that the effect of the Be exit window, often included in the X-ray tube design as a first filter and different additional thicknesses of Al and Cu filters can be effectively used to attenuate low energy photons, often responsible for high dose inhomogeneities in thick samples. To assess the feasibility of using the available X-ray spectra for the irradiation of different samples having thicknesses up to several millimetres, the absorbed dose across the sample's depth for different materials such as Radio Photoluminescent (RPL) glass dosimeters, silica for comparison purposes, and water as reference was calculated using PHITS, with a sample depth spatial resolution of 0.1 mm and 10 μm The homogeneity of the absorbed dose in the RPL dosimeter volume can be improved by the use of appropriate types of filters and it is found that 1.5 mm, 3 mm thick Al and 1.5 mm thick Cu filters can improve the dose homogeneity to 30 %, 15 %, and 8 % deviation from the average dose value respectively in the selected samples. By using a combination of the readout of PTW soft X-ray ionization chamber, normally used for dose rate calibration in the irradiation facility, and the realized simulations, the absorbed dose was calculated for 8 RPL glass samples irradiated in the MOPERIX X-ray irradiator in the frame of another study. The calculated doses are in good agreement with the corresponding experimental values, which were measured in the European Organization for Nuclear Research (CERN's) readout systems, allowing a validation of the used methodologies and the estimation of usable conversion factors.

Keywords*: X-ray tubes, Monte Carlo, PHITS, Radiation, Matter, Radio - photoluminescence, Dosimetry.*

Declaration

I am an Erasmus Mundus Joint Master's Degree Student in "Radiation and Its Effects on Microelectronics and Photonics Technologies" student at three different higher institutions in Europe such as University of Jyvaskyla – Finland, Ku Leuven University – Belgium and University of Jean Monnet – France.

I have completed my internship and master's thesis work at the University of Jean Monnet on the title" Dosimetry Study in an X-ray Irradiator: Monte Carlo Simulations and Experimental Results on RPL Samples" (from March 01, 2023 – July 21, 2023).

I declare that this report is my original work that includes the information gained from the intern place, my own simulation results, experimental results, and what I have accessed in different books, journals, and conference papers.

Student Name
Abrham Kassa Alem

Acknowledgment

At the very beginning, I would like to express my deepest gratitude to the almighty God for giving me the strength to accomplish my internship and prepare this report. It has been great to be working as an intern which really helped me to upgrade my theoretical knowledge and develop a new set of skills. For this opportunity, I would like to give gratitude to:

My supervisor, Professor Matteo Ferrari for his advice and guidance on how to approach and handle situations, his guidance, and his valuable comments on the report writing process.

Ygor Aguiar from CERN for the collaboration work in the experimental measurements which were done at CERN and sharing the results.

Lorenzo Sostero from the University of Brescia, Italy for the collaboration work and discussions on the possible methodologies of the work.

I also appreciate Professor Sylvain Girard and all MOPERE research team members for their collaboration and valuable comments regarding the work and collaborations during the experimental irradiation campaigns. Then last but not least, I thank the PHITS Office from the Japanese Atomic Energy Research Agency for giving me the license for PHITS software and for their quick email reply in case of questions regarding software bugs.

Table of Contents

Table of Figures

List of Tables

List of Acronyms

Al	Aluminum
CERN	European Council for Nuclear Research
Cu	Copper
DUR	Dose Uniformity Ratio
EGS5	Electromagnetic cascade version 5
LabHC	Laboratory Hubert Curien
MOPERE	Materials for Optics and Photonics in Extreme Radiation Environments
PHITS	Particle Heavy Ion Transport Code System
RPL	Radio Photoluminescent

Chapter 1

Introduction

This section of the study presents a short and simplified description of the interaction between charged and neutral particles with matter, with a particular emphasis on the production of X-ray photons resulting from charged particle interactions with matter. Additionally, the generation of secondary radiation resulting from of X-ray photon interactions with matter is presented. The produced X-ray photons are utilized to investigate dosimetry in various samples, as described in Section 2.4.

The exposure of matter to ionizing radiation leads to a variety of interactions. These interactions are also prone to inherent fluctuations, which are a direct result of the quantum nature of both matter and radiation [1]. According to [1] the quantities that describe the fundamental processes of energy transfer can be classified into non-stochastic and stochastic quantities. A non-stochastic quantity has a unique and deterministic value. On the other hand, a stochastic quantity has a nondeterministic value, and a probability distribution is typically associated with it. The interaction of radiation with matter generally leads to excitation and ionization. Ionization is a process that liberates one or more electrons in the interactions of particles with molecules or atoms [1], [2]. Excitation consists of the transfer of energy to atomic electrons, allowing them to occupy higher energy levels in atoms or molecules and relatively require less energy in comparison to ionization for the same atom or molecule [2].

Charged particles (such as protons, electrons, alpha particles), high energy photons (gamma and X-ray radiation), and neutrons as well are among the most commonly known types of ionizing radiation. Because of their distinct interaction mechanism with matter, charged and neutral particles are generally classified as directly and indirectly ionizing radiation, respectively. Directly ionizing radiation entails charged particles that then can directly transfer their energy to matter for example through numerous Coulomb interactions forming a particle's track [2].

By contrast, indirectly ionizing radiation refers to neutral particles (such as photons, and neutrons) that deposit energy whenever in correspondence of discrete events that leads to the production of charged particles.

Additionally, the interaction of uncharged particles is discrete, via events alternating to relatively long paths in matter without any direct interaction as they are neutral. So, the energy deposited by neutral particles comprises the production of charged secondary particles in the medium as a first step. Photons commonly produce secondary electrons or positrons, and neutrons can release protons or heavier ions as secondary charged particles. In the subsequent step, the liberated charged particles transfer energy into the medium via Coulomb interactions with the orbital electrons of the constituent atoms [2].

1.1 Interaction of Electrons with Matter

Electron-matter interaction can lead to radiative or collisional loss, the later including ionization and excitations, as mentioned in [2]. It is worth noting that the present discussion is limited to electron interactions that contribute to the formation of X-ray photons, which correspond to the application studied in this work.

1.1.1 Characteristics X-ray Production

Electrons, via collisions, can ionize an atom, creating a vacancy and allowing a re-arrangement leading to the emission of a so called characteristic X-ray. These characteristic X-rays are produced as a result of electronic transitions in atoms that correspond to vacancies in the inner electronic shells of the absorber atom. The photons emitted due to the electronic transitions are known as characteristic radiation. This term is used because the wavelength λ and so the corresponding energy hν of the emitted photon are unique to the emitting atom. Even though it is an outdated term, fluorescence radiation is still sometimes used to describe characteristic photons [2]. The line spectrum of the atom [3], [4] is the collection of discrete radiation transition photons released by a specific atom as shown in the Figure 1. In this simplified scheme, the pink dots represent incident electrons as well as the electrons that surround the nucleus of the atom which is composed of protons and neutrons. When the electron is incident in an atom, the electrons from the inner shell can be removed from the atom or excited to the outer shell orbitals and leave a vacancy space. This vacancy space can be filled by electron from higher energy level and this produce characteristics X -rays.

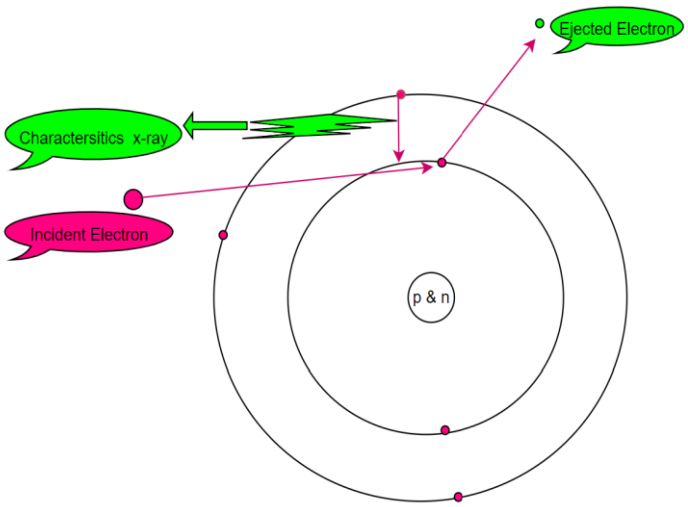

Figure 1: Schematic Diagram for Characteristic X-ray Production.

1.1.2 Bremsstrahlung X-ray Production

The production of Bremsstrahlung X-rays is a result of inelastic Coulomb interactions between the nucleus of the absorber atom and highly energetic charged particles. The production of Bremsstrahlung photons is directly proportional to the square of the atomic number of the medium and inversely proportional to the square of the particle's mass [4]. As a result lighter particles generate more Bremsstrahlung X-rays compared to heavier particles. Electrons are frequently used for X-ray generation, and the produced X-ray spectrum results from the sum of two components: the characteristic X-ray peaks and Bremsstrahlung X-ray spectra [4]. As shown in Figure 2, the pink dots represent incident electrons and the electrons that surround the nucleus of the atom which is composed of protons and neutrons. When the electron is accelerated towards the nucleus, it is deflected by the field of the nucleus and some of its kinetic energy is converted into photons. In the MOPERIX-UJM facility studied in this work, X-ray spectra are produced using a commercial X-ray tube (the details of the tube are explained in Chapter 2) by accelerating electrons on a tungsten target. For the simulations, in this present work, X- ray spectra are produced by using electrons and allowing them to interact with a tungsten target through the use of particle transport software tools, as detailed in Chapter 2.

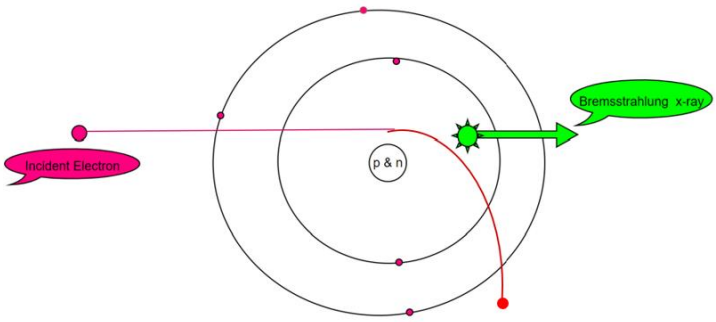

Figure 2: Schematic Diagram showing the production of Bremsstrahlung X-ray photons.

1.2 Interaction of Photons with Matter

The main interaction processes of photon radiation with matter consist of Photoelectric, Compton scattering, and pair Production [5]. In the study of collision dynamics of particles, the particle sources are commonly referred to as projectiles, and any matter where all projectiles interact with it is typically referred to as a target. Whenever there is particle-matter interaction, there is at least either a change in the energy of the projectiles (inelastic or incoherent scattering) or a change of direction of the projectiles (coherent or elastic scattering).

1.2.1 Photoelectric Effect

Photoelectric effect is observed when a photon of a given energy is absorbed predominantly by the inner shell electrons, causing the electron to acquire sufficient energy to be expelled from the atom. As the inner shell electrons are tightly bound to the parent atom of matter, the photon energy must be roughly equal to or greater than the ionization energy of the inner shell electrons for the photoelectric effect to occur [2]. Depending on the energy of photons, the photoelectric cross-section is greatly dependent on the atomic number (proportional to the fourth power of the target atomic number for low-energy photons or the fifth power of atomic number for high-energy photons [5].

1.2.2 Scattering of Photons

The scattering of photons can be of coherent or incoherent scattering. At photon energies lower than 10 keV, coherent or elastic scattering such as Rayleigh scattering, in which the produced scattered photon has identical energy as the incident one, is possible as well [5]. The cross-section for coherent scattering is proportional to the ratio of the target atomic number to the square of the energy of the photons [4], [5]. On the other hand, Compton scattering is a type of inelastic scattering that occurs when a photon with a given energy interacts with a single electron of the target, and it produces a photon whose energy is lower than the energy of the incident photons. The cross-section or interaction probability of the Compton scattering is inversely proportional to the energy of the incident photon energy [5].

As shown in Figure 3, a fraction of the energy of the incident photons is transferred to a recoiling electron in the form of kinetic energy and the resulting photon scatters in a certain direction. The collision dynamic of Compton scattering is expressed mathematically by equation (1) [4].

$$E_f = \frac{E_i}{[1+(1-cos\theta)\frac{E_i}{0.511}]} \quad (1)$$

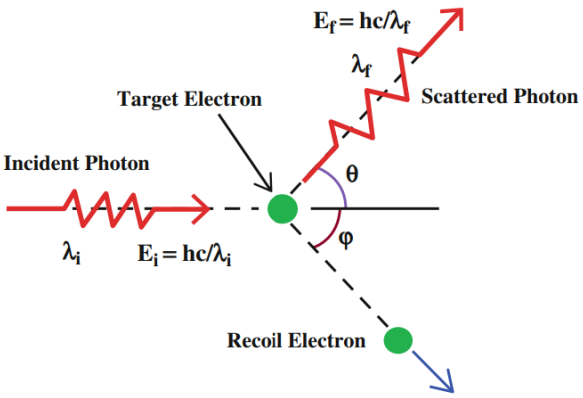

Figure 3: Schematic Diagram showing principles of Compton Scattering : Image adapted from [4].

Where E_f, E_i , θ, φ , $\lambda_{i,}$, , $\lambda_{f,}$ c *and* h *are* the scattered photon energy, the incident photon energy, the photon scattering angle , the recoil angle for the electron , the wavelength of the incident photon, the wavelength of the scattered photon , speed of light and Planck's constant respectively.

1.2.3 Pair Production

Photons with a minimum energy of 1.022 MeV and 2.04 MeV as shown in Figure 4, can produce electron-positron pairs in the field of the nucleus and in the field of electrons respectively [6].

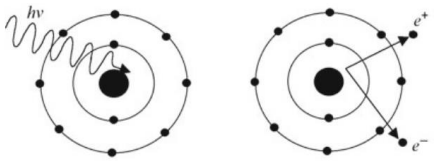

a) b)

Figure 4: Schematics showing Pair Production Phenomena in the field of nucleus: a) Before interaction, b) after interaction: Image adapted from [2].

Photons with energy higher than 2.04 MeV may also undergo photonuclear reactions in which they are absorbed by a nucleus and resulting in the production of protons, neutrons, or other heavy ions [6]. Considering all the described phenomena, the energy conversion between photons and electrons is a multifaceted process that normally generate a cascade of events, as summarized in the flow chart shown in Figure 5.

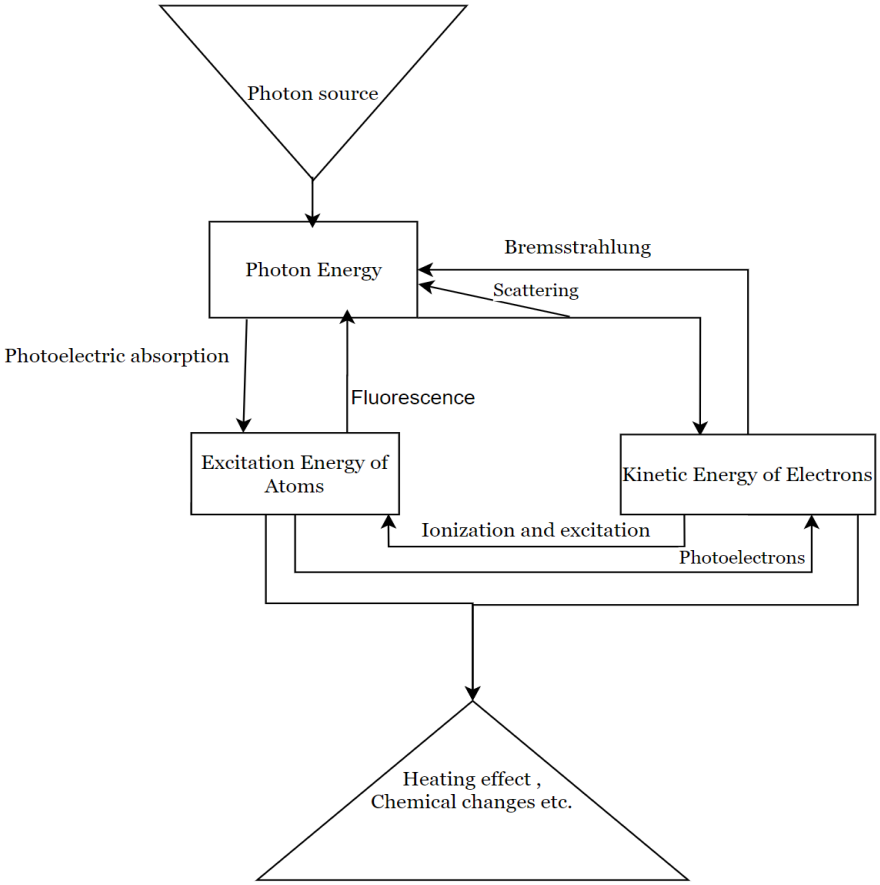

Figure 5: Possible mechanisms of energy conversion during the process of photon energy interaction with matter. Image adapted from [5] and customized into our case based on the maximum energy of photons available in the used X-ray Irradiator.

Figure 6 summarizes the relative importance of the three processes described so far as a function of the energy of the incoming photon and as a function of the Z of the target material. The photoelectric effect is also energy and atomic number dependent, and it is dominant until 0.5 MeV energy for high atomic number materials. MeV energy range for light materials (Z up to about 20), and pair production is dominant starting from 10 MeV photon energy.

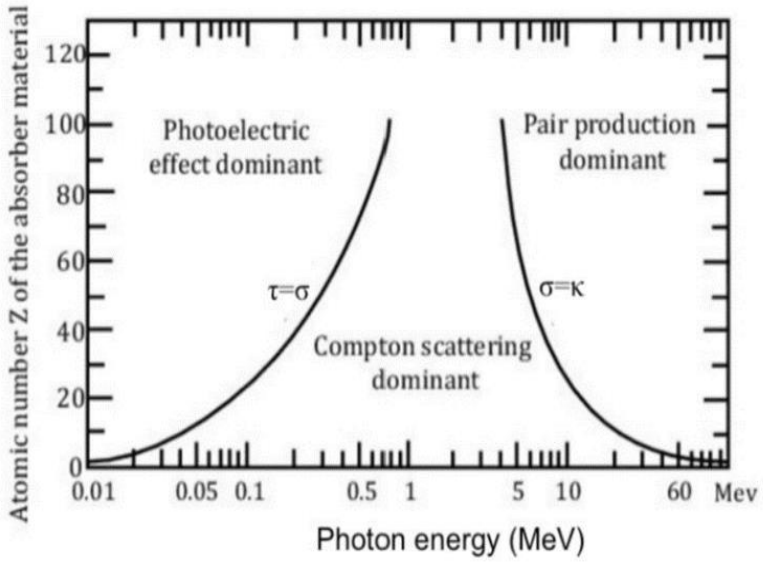

Figure 6*:* Photon-matter Interaction*:* Image adapted from [6].

For different photon interaction mechanisms, the overall interaction cross-section which is expressed by equation (2) is important to study the radiation effects on materials and dosimetry applications [5], [6].

$$\sigma_{tot}=\tau_{pe}+\sigma_C \qquad (2)$$

where the interaction $\sigma_{tot}, \tau_{pe}, \sigma_C$ are the total cross-section, photoelectric cross-section, and Compton cross-section, respectively. Considering the scope of the present work, the cross section for pair production, photonuclear and Rayleigh scattering are neglected in this work.

1.2.4 Exponential Attenuation

When photons with a certain energy pass through a slab of material, the incident photons can pass through the medium without any interaction, or it can be scattered or absorbed by the medium. Hence, the intensity of the primary photon beam while penetrating the target material progressively attenuates.

Mathematically speaking, in simplified geometry conditions, the intensity of the primary beam interacting with a homogeneous medium with thickness 't' can be expressed using the following equation (3) [5].

$$I(t)=I_0\, e^{-\mu t} \qquad (3)$$

Where I(t), I_0, t and μ are the beam intensity at thickness t, the incident photon intensity, the thickness of the medium, and the attenuation coefficient respectively. The mass attenuation coefficient (μ/ρ) is an important factor in the study of photon-matter

interaction and it is the attenuation coefficient normalized by the density of the medium. If the medium is a mixture or a compound, the mass attenuation coefficient will be the average weight of all the constituent elements as it is written in equation (4) in [2],[4], [5]:

$$\mu/\rho = \sum_i w_i \, \mu_i \, /\rho_i \qquad (4)$$

Where w_i is the i^{th} elemental constituent proportion by weight. Before discussing the Monte Carlo simulations, it is better to understand the interaction of photons with matter and then the physics behind absorbed dose estimations as well as dosimetry concepts. This is detailed in the following Section.

1.3 Dosimetry

Dosimetry is defined as the quantification of the absorbed electromagnetic or particle radiation energy on matter [1]. The significance of dosimetry in the field of radiation science, particularly in the domain of medicine, was recognized at an early stage, as demonstrated by the inception of the International Commission on Radiation Units and Measurements (ICRU) as early as 1925 [1]. One of the most important physical quantities used in radiation effects assessment is the physical absorbed dose which is defined as the expectation value of the energy absorbed per unit mass, and its SI unit is gray (Gy). The absorbed dose quantification is dependent on the type of incident ionizing radiation. For example, in the case of indirect ionizing radiation such as photons, the deposition mechanism depends on the interaction of photons with matter and on the generated secondary electrons and their following transport in matter as well. An example of possible interaction and energy deposition mechanism for two different photons entering a spherical volume of a generic material is shown in the schematics reported in Figure 7. Incident photons impinge on a spherical volume of a given material. The photons crossing the sphere may pass through a certain depth of matter without interacting, may transfer part, or even all of their energy to electrons and may be scattered out of the sample volume. The secondary electrons may in turn directly contribute to the sample dose depositions or may also produce Bremsstrahlung photons through coulomb scattering with the medium Their energy can be fully deposited in the sphere, or they can leave the sphere carrying out a certain fraction of their initial kinetic energy. Many more complex cascading events can take place during the interactions. The incident photons can even produce secondary electrons before entering the sphere, and these electrons can contribute to the dose deposited in the sphere, depending on their energy and the corresponding range in matter.

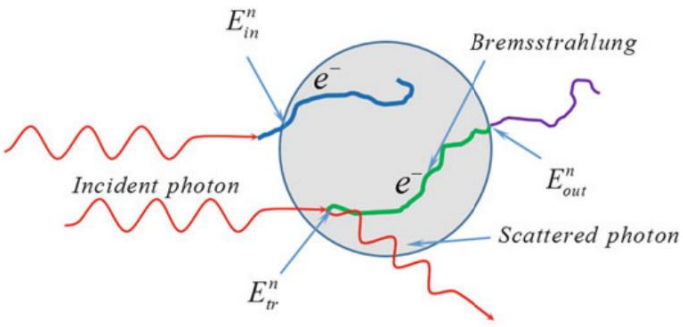

Figure 7: A schematic illustration of the possible events generated by photons interacting with a sphere of generic material and examples of the produced secondary electrons. Image adapted from [4].

The energy imparted ε to the volume of interest can be expressed by the following equation:

$$\varepsilon = E^n_{tr} - E^n_{out} + E^n_{in} \quad (5)\ [4]$$

Where E^n_{tr}, $E^n_{in,}$, E^n_{out} are the energy transferred from photons to secondary particles (electrons in this case), net kinetic energy of electrons that enters to the volume, and net kinetic energy of electrons that leaves the volume respectively. In the case the energy of charged particles entering the volume of interest is equal to the energy of charged particles leaving the volume ($E^n_{out} = E^n_{in}$), this condition is known as charge particle equilibrium. At charge particle equilibrium, the absorbed dose is equal to kinetic energy transfer (KERMA). For mono-energetic photons, the absorbed dose at equilibrium can be obtained from equation(6) [2], [4]:

$$D^{CPE} = \left(\frac{\mu_{en}}{\rho}\right) E\varphi \quad (6)$$

Similarly, for photons with energy distribution ranging from 0 to E_{max} :

$$D^{CPE} = \int_0^{E_{max}} E\ \Phi_E \left(\frac{\mu_{en}}{\rho}\right) dE \quad (7)$$

$$\frac{\mu_{en}}{\rho} = \frac{\mu}{\rho}\frac{\bar{E}_{ab}}{E_v} \quad (8)$$

Where D^{CPE} = dose at chare particle equilibrium

$\frac{\mu_{en}}{\rho}$ = Mass energy absorption coefficient

E = incident monoenergetic photon energy

φ= fluence for monoenergetic incident photon

E_{max}= maximum Energy incident photons

Φ_E= fluence of a heterogeneous energy incident photons

$\frac{\mu_{en}}{\rho}$ = mass energy absorption coefficient

$\frac{\mu}{\rho}$ = mass attenuation coefficient

$\overline{E}_{ab}$ = mean absorption energy

E_v = incident photon energy

1.3.1 Monte Carlo Fundamentals

As previously mentioned, the stochastic character of radiation-matter interactions necessitates the use of general Monte Carlo-based particle transport tools for dosimetry calculations in real-life configurations. These Monte Carlo tools are used for the estimation of physical quantities of interest, also referred to as tallies in some codes. For example, the particle fluence in a volume of interest, the number of secondary particles or yield, the absorbed dose in a reference volume, particle trajectories, and numerous other quantities and parameters can be estimated by utilizing known probability distributions and the generation of random numbers.

Thanks to different types of physics models that can be used for the transport of different particles in various energy range, different sets of available cross-sections library databases are accessed by Monte Carlo codes and can be selected by the user depending on the specific simulated situation.
A schematic example of the operation mechanisms of a Monte Carlo simulation is illustrated in Figure 8. As discussed in the previous sections, when a particle enters a given volume of material, it can interact and produce different secondary radiations. Monte Carlo simulations can follow the transport of the primary particle and of all the produced secondaries, and this process continues until the particle exit the defined geometry, it is absorbed, or when the remaining energy falls below the minimum energy threshold. Accordingly, the transport of particles depends on the type of materials and their densities, on the specific geometry and its physical dimension, and on the elements surrounding the volume of interest as well. Quantities of interest are estimated by Monte Carlo codes by averaging the value scored by each particle history (primary and then their secondaries, whose contribution is properly weighted) normally over a high number of primaries. The estimated physical quantity of interest in the case where no variance reduction technique for computational simulation efficiency improvement is used, can be mathematically written in equation (9) [7].

$$\bar{Q}=(\sum_1^N Qi)/\mathrm{N} \qquad (9)$$

Where $\overline{Q}$ is the estimated quantity of interest, N is the number of particle showers, and Qi values scored by ith shower. Shower is a cascade of particles which are created by an energetic incident particle. Each of the particles generated in a shower can contribute to the overall dose deposition.

Qi $=(\sum_{j=1}^{n} Q\mathrm{ij})/\mathrm{n}$, Qij is the dose contribution by the jth particle of the shower.

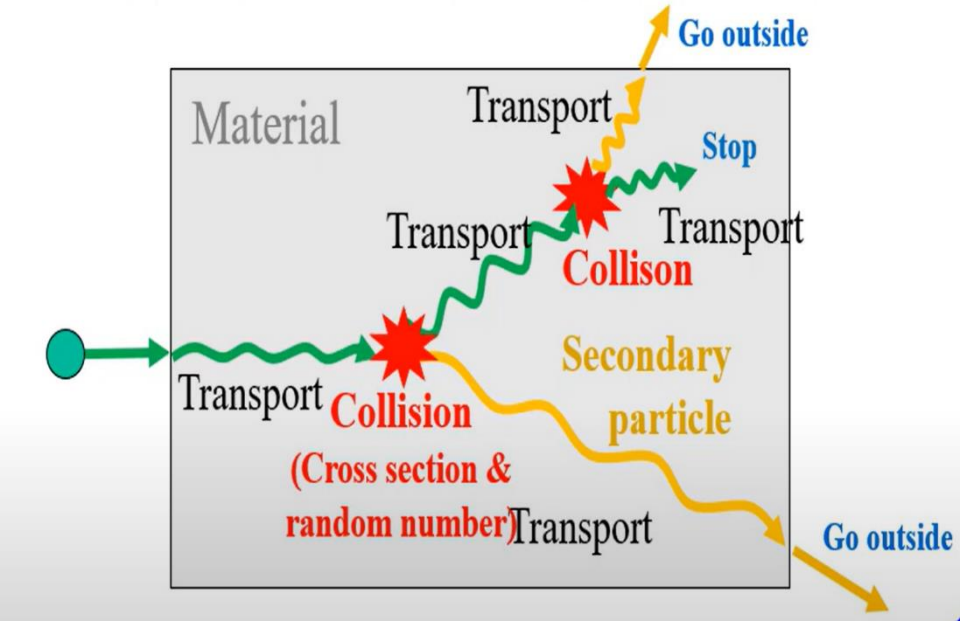

Figure 8: Example of particle Transport: Image Adapted From [8].

1.4 Aim of the Study

The main goal of this study is to simulate a commercial (COMET165) X-ray irradiator, usually referred to as MOPERIX, that is used in the Hubert Curien Laboratory of the University Jean Monnet (UJM) of Saint-Etienne, for irradiation testing experiments. Its maximum operating tube potential is 160 kV, and the maximum photon energy is determined by its tube voltage. So, photons with energies up to 0.16 MeV are produced (but actually most of them have lower energy as shown in Section 3.1). The X-ray tube is traditionally used at a maximum tension of 100 kV [3].

Final aim of the work is the dose deposition study in various samples of interest irradiated with X-ray radiation. In particular, the depth dose distribution is analysed for Radio photoluminescent (RPL) glass rods (GD-301) that are irradiated in the frame of another research study. Furthermore, the study of dose distribution along these various samples depth under different X-ray tube potentials and the irradiation feasibility in these specific samples and in the specified irradiation conditions is planned using various filters, aiming at improving the homogeneity.

1.5 State of the Art

To orient this work, previous similar studies were analysed. Simulation of the dose deposition in silver-containing glasses, specifically silver-containing zinc phosphate glass and silver-containing Gallo phosphate glass have been studied in [3] using Geant 4 Monte Carlo code. In both types of glasses a dose reduction corresponding to the depth within the material is reported [3]. In another work, the dose deposited in the core, coating, and cladding of phosphorus-doped optical fibers were compared using Geant 4 simulations [9]. X-ray photon energies of 30 keV were found to significantly contribute to the total deposited dose in these samples [9].

These low-energy photons are responsible for a higher dose depositions in the sample layers closer to the surface. This may cause significant dose inhomogeneities.

Concerning medical applications, for whole-body and long-leg X-ray imaging examinations, studies also showed that 14 mm thick Al or 14 mm Al combined with 1 mm thick Cu as a composite material can be used to improve X-ray image signal-to-noise ratio by 46 % and significantly reduce the undesired dose to the patient [10]. Based on these considerations on the effect of different types of filters and their thickness on average dose reduction, the doses absorbed by different samples and their inhomogeneities corresponding to the use of different thicknesses of Al and Cu filters are studied. The realized models include the X-ray tube geometry and the effects of the built-in Be filter on the X-ray spectrum as well.

Chapter 2

Methodology

In this investigation, a model of the X-ray irradiator available at the Hubert Curien Laboratory is realized using PHITS, a general Monte Carlo code used in the frame of this work. Further detail on PHITS is provided in section 2.1. The characterization of the used X-ray spectra, is assessed simulating relevant quantities such as the photon fluence as a function of photon energy, in different irradiation conditions. For example, the impact of different filters on the photon energy spectrum is studied.

The effect of the Be window which is part of the X-ray tube as a primary layer filter, and different thickness Al and Cu filters are considered as an additional secondary layer filter to evaluate their impact on the dose inhomogeneity in various sample geometries. The spectra outcomes studied in PHITS are compared with SpekPy software [11], which is a Python-based tool primarily used in the design of an X-ray tube at various filter types and photon emission cone angles. This SpekPy software is commonly utilized in medical physics applications and its photon spectra have been verified through experimental measurements.

The dose distributions as a function of the sample depth are evaluated to estimate the dose inhomogeneities within different sample volumes and materials, such as RPL glass, silica, and water. Dosimetry in different photon spectra is studied.

Finally, simulations are used to determine calibration factors to convert the dose readout in water, as provided by the ionization chamber normally used for calibration in the X-ray tube, to the dose absorbed by specific samples made of RPL glass and silica. This calibration factor has been experimentally confirmed by CERN's readout on RPL dosimeters, within the framework of a research project executed in collaboration with CERN. In the following sections, the details of the methodology starting from what PHITS Monte Carlo is, how the X-ray tube is designed and the investigation of different simulation setups to see the computational feasibilities of dosimetry are detailed.

2.1 PHITS General Monte Carlo Code

The Monte Carlo Code *Particle and Heavy-Ion Transport System* (PHITS) is a tool for the simulation of particle transport and interaction in three-dimensional models. This versatile general Monte Carlo code has been developed in the frame of a collaboration including the Japanese Atomic Energy Agency (JAEA), and several other institutes [12]. The code is used in various research and development fields where radiation is present, including shielding design for radiation protection applications [12]–[17], cosmic ray research [12], medical physics [13], [14], [18], [19], [20], design of accelerators, nuclear technology and radiation effects on materials studies [15]–[17].

Different physics models optimized for specific particles and energy ranges are implemented in PHITS. They are developed to properly model the transport of specific particles and to access the most appropriate interaction cross-sections, which depend

indeed on the type of particle and the considered energy range. Based on the specific analysed phenomena, the most suitable physics model can be selected. Figure 9 shows the types of different physics libraries used in PHITS for the transport of different particles with different energy ranges.

The simulations discussed in the present work are achieved using PHITS version 3.3, using the EGS5 physics model, the most indicated for the transport of photons and electrons in the energy range of interest for this study, as shown in Figure 9.

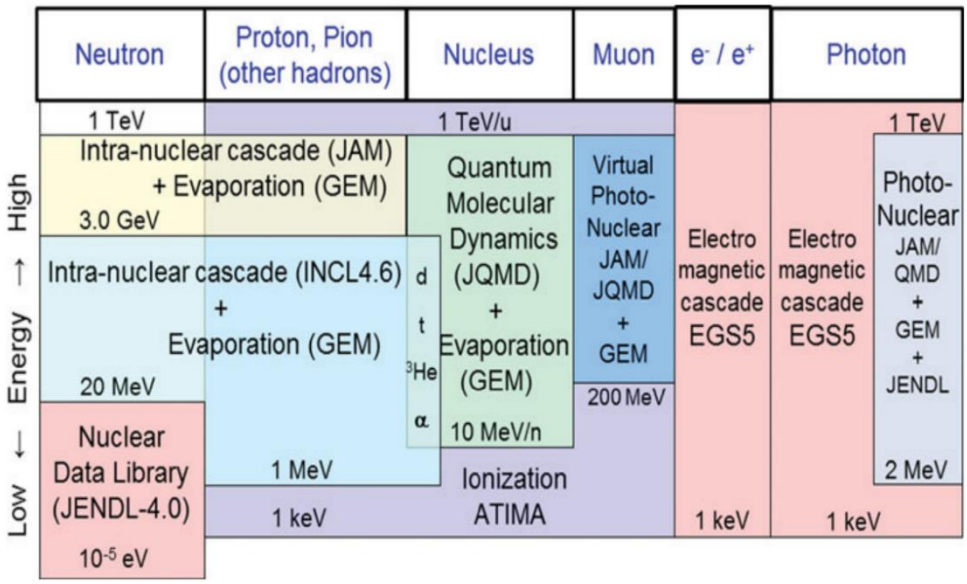

Figure 9: PHITS Physics models for simulating atomic collisions and nuclear interactions, Image adapted from [15].

2.2 Description of the X-ray Tube Available at LabHC

In the frame of this work, PHITS was used to simulate the photon spectrum produced by a commercial X-ray tube, whose operation principles are briefly described here. A standard X-ray tube is made of a cathode, an anode, which acts as a target, and a beryllium exit window. Electrons are emitted from the cathode, which is made of a metallic filament, through a thermionic emission process and then accelerated toward the anode [9], [22]. The anode, on the other hand, is made of high melting point and dense elements. Traditionally, tungsten (W), rhodium (Rh), and molybdenum (Mo) anodes are used as target materials. Different types of targets can be used in different application areas [9], [23].

The orientation of the target with respect to the vertical axis, perpendicular to the electron beam direction, influences the photon fluence in the desired direction. Generally, the photon fluence has to be maximized in the direction perpendicular to the electron beam. To this purpose, the optimized angle between the target surface and the vertical surface has been studied to correspond to 30 degrees [22].

As shown in a simple schematics in Figure 10, an example of X-ray tube in which the electrons impinge the target in a specified region, the target angle used is 30 degrees, and the photon emission angle is 40 degrees [9]. However, the irradiator that is modelled in this work has the following specifications: its photon emission angle is 50 degree, and its Be exit window thickness is 4 mm. The specifications of X-ray irradiator (Comet MXR -165) modelled in this work are summarised in Table 2. This irradiator is a specific commercial X-ray tube available at the LabHC where experimental irradiations are extensively performed, and for this reason, a PHITS model of the facility is needed to verify the feasibility of the irradiation of different samples with different tube potentials and shielding materials.

Target Angle	Emission Angle(α)	Target Element	Exit Window	Nominal tube voltage
30°	50°	W	4mm thick Be	160kV

Table 1: X-ray Irradiator(Comet MXR -165) Specifications [24]

The electron source and anode are kept under vacuum to minimize any interactions with air prior to reaching the intended target. The described irradiator has been extensively used to perform experimental activities, mostly concerning the irradiation of Optical fibers and other Photonic technologies, examples can be found in [3], [9]. In these studies , the irradiators have been mostly operated at a standard tube potential of 100 kV. The maximum available current associated to this tube potential is 45 mA. However, the tube can be operated up to a maximum of 160 kV, with a maximum current of 28 mA.

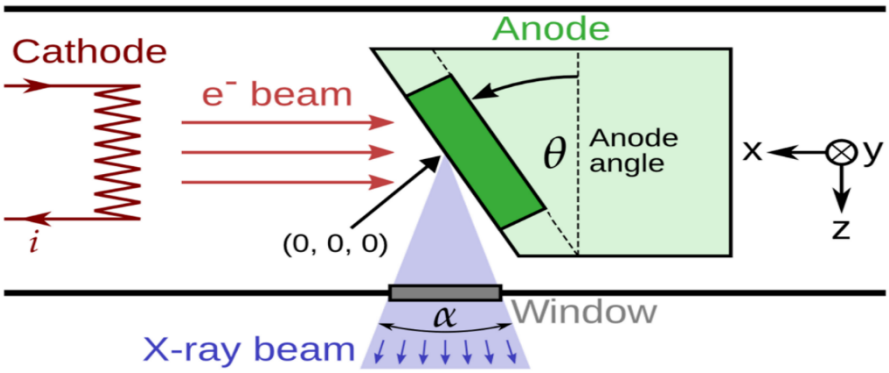

Figure 10: X-ray Irradiator Schematic Design, Image adapted from [9].

2.3 PHITS Model of the X-ray Tube

A pencil electron source is used to model the electrons emitted from the cathode [22], [23] and directed towards the tungsten target. When a 100 kV tube voltage is used, a monochromatic pencil electron beam with energy (E =100 keV) impinge on the W target. In PHITS general Monte Carlo tool, parameters such as number of primaries, transport modality for photons, electrons, and positrons, with minimum threshold energy for electron transportation (emin = 0.1 keV) are all activated.

In the simulation, the target and the Be window are enclosed in a 4 mm thick lead (Pb) structure surrounding the target and adequately shaping the desired emission cone of the produced photons. A 4 mm thick cylindrical Be exit window, that in the model has a radius of 18.65 mm, is utilized to filter out low-energy photons. Tally regions are also defined to compute the photon fluence spectra prior to and following the Be filter. These tally regions are of the same size as the filter and they are made of air. In PHITS, each defined volume is described using the chemical compositions, geometry, and density of its material. In this present work, the materials and their corresponding densities used for the simulations of X-ray tube are reported in Table 3.

The target is modelled using a parallelepiped volume (RPP box) made of tungsten with 50mm thickness; this volume is cut by a plane described by the general plane equation Ax+By+Cz+D=0, where the plane parameters A, B, and C are possible combinations of coordinate points and D is a constant. This cutting plane is used to set the desired target angle in the geometry. As previously mentioned, the target angle is calculated mathematically by considering the angle between the Z-plane and the cutting lane using the equation below: Z-plane: $C_1 = 1$, D_1 =Constant. The cutting Plane: 0.58x + z = 0; where A = 0.58, B= 0, C= 1, and D= 0, and the cosine of the angle between the two planes is determined mathematically using the angle between two geometrical planes and the designed tube as shown in Figure 11. From this figure i), the lead box is not shown to make the target visible. The tungsten target (indicated by W and represented in purple), tally region to measure the simulated photon fluence as well as the Beryllium exit window indicated by Be are included. In the figure on the right side (Figure 11 ii), the following elements can be identified: the lead box indicated by (Pb) and represented in green, used to enclose the target as well as particle sources, the Be window on the exit side and an outside tally region used to measure the photon fluence after the Be filter. The target and the source are inside a vacuum region which is implemented using a void region in PHITS.

Material	Atomic Number	Density (g/cm^3)
Air (~ 80 % *N* and 20 % O)		1.225e-3
Tungestun (W)	84	11.20
Beryllium (Be)	4	1.848
Lead (Pb)	82	19.25

Table 2 : Atomic Composition of Materials Used for X-ray Generator Design in PHITS Simulation.

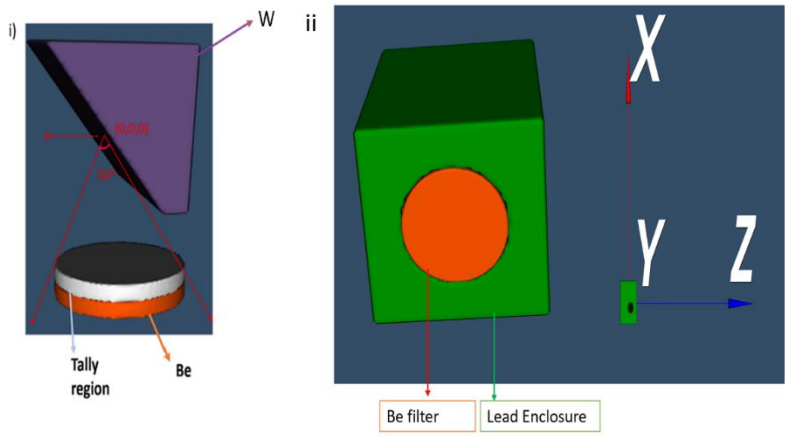

Figure 11: X-ray Tube Geometries 3D View.

i) 3D Geometries inside the tube (COMET MXR-165, ii) 3D Tube geometry seen from the front side. The orientation of the axis for figure i) is also the same as the one indicated in the second figure.

2.4 Dosimetry Simulation Setup

The use of an electron source to simulate the X-ray production in the W target leads to simulations in which the computational time is critically long, due to the high number of interaction of electrons with matter [7]. Accordingly, a second set of simulations where realized by replacing the electron beam with a photon source replicating the X-ray spectra exiting the target, aiming at improving the efficiency of the simulations and saving computational time.

X-ray spectra previously generated through the interaction of an electron source with the tungsten anode target or produced by Spekpy can be used to this purpose. As discussed Section 3.1, PHITS was found to underestimate the characteristic contribution to the X-ray spectra when compared with Spekpy, and this justifies the use of X-ray spectra simulated by SpekPy software for the realization of a new photon source. In this case, the simulated source is polychromatic energy beam, isotropic, and correspond to a point photon source placed in the origin of the coordinate point as shown in Figure 12. A 1.5 mm thick Al filter is also introduced at 4 cm far from the source and the samples are placed at approximately 1 cm below it. All of these parameters were implemented in the PHITS source definition section.

2.4.1 RPL Sample Used for Dosimetry Simulations

The studied samples are cylindrical rods with a diameter of 1.5 mm and a length of 8.5 mm. This type of glass is used as a dosimeter in mixed radiation environments such as for high-dose applications at CERN [25] and boron capture neutron therapy applications [25]–[29]. RPL dosimeters are composed of silver-doped phosphate glass.

Its fundamental operational principle is beyond the scope of the present work and can be found in references [25]–[27]. The silver atoms that are doped in the phosphate glass are reliably and uniformly present as Ag^{+} ions. Upon ionizing radiation exposure of this

glass, electrons from the valance band are emanated to the conduction band and then trapped by silver ions so as to form stable RPL luminescent centers (Ag^{o}). These centers can also arise from the migration of holes through the glass, which combines with Ag^{+} ions to form Ag^{++}. When exposed to UV light, RPL centers (Ag^{o} and Ag^{++}) emit orange luminescence whose intensity is proportional to the deposited dose. If the annealing conditions are not met, Ag^{o} and Ag^{++} centers will not revert to the Ag^{+} state. This allows the possibility of having multiple readouts of RPL detectors without any impact on the signal [28].

	Density [g/cm^3]	O [wt-%]	P [wt-%]	Na [wt-%]	Al [wt-%]	Ag [wt-%]
FD7	2.6041	51.16	31.55	11.0	6.12	0.17

Table 3: RPL Glass Material Compositions [25].

In the simulations, silica glass and water with densities 2.2 $g/\text{cm}3$ and 1 $g/\text{cm}3$ respectively are used as well for comparisons.

RPL sample geometry has been initially approximated as a rectangular box, whose physical dimensions are 8.5 mm longitudinally on the z-axis, 1.5 mm on the y-axis, and 1.5 mm in thickness along the x-axis. Subsequently, to compute the dose distribution as a function of the sample depth, the sample geometry is partitioned into fifteen 0.1 mm thick identical slabs as shown in Figure 12. Each of the slabs is defined as a cell in the PHITS geometry.

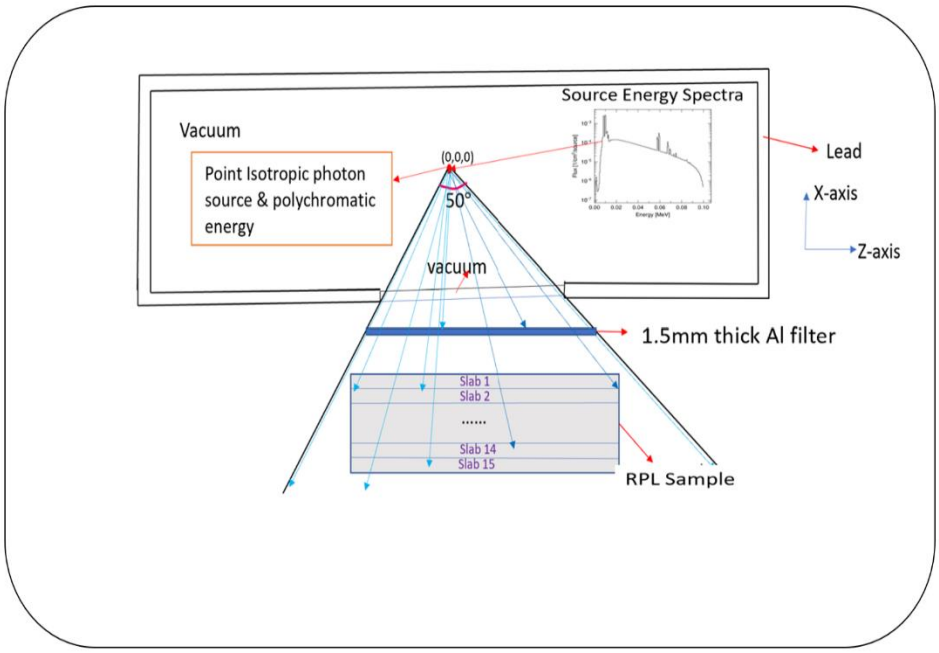

Figure 12: Dosimetry Simulation Setup Schematics.
All the dimensions used are not in the right scale.

2.4.2 PHITS Tally Functions

PHITS scores to compute quantities of interest are referred to as 'Tallies'. *T-Track* tally is used to compute particle fluences and particle trajectories [12]. Then *T-Deposit* tally is used to compute the dose deposited in various slabs of the RPL sample, water and silica in the same simulation conditions. The *T-Deposit* tally employs mesh voxels to compute the dose distribution in the samples. The sample is positioned 5 cm far from the source as shown in Figure 13.Then the average dose absorbed by the RPL sample was simulated by considering the whole sample volume for both cylindrical and rectangular box sample shapes to compare the two types of shapes. The results, as reported in Section 3.2.3 showed minimal variations, justifying the use of the approximated rectangular box shape for the simulation. As shown in Figure 13, tally regions to calculate the photon fluence variations before and after the filter are also used. The RPL sample geometries in 3D is shown in purple colour and indicated by 'RPL sample' from the designed tube. The tube geometry is used to keep the emission cone of photons in the direction of interest.

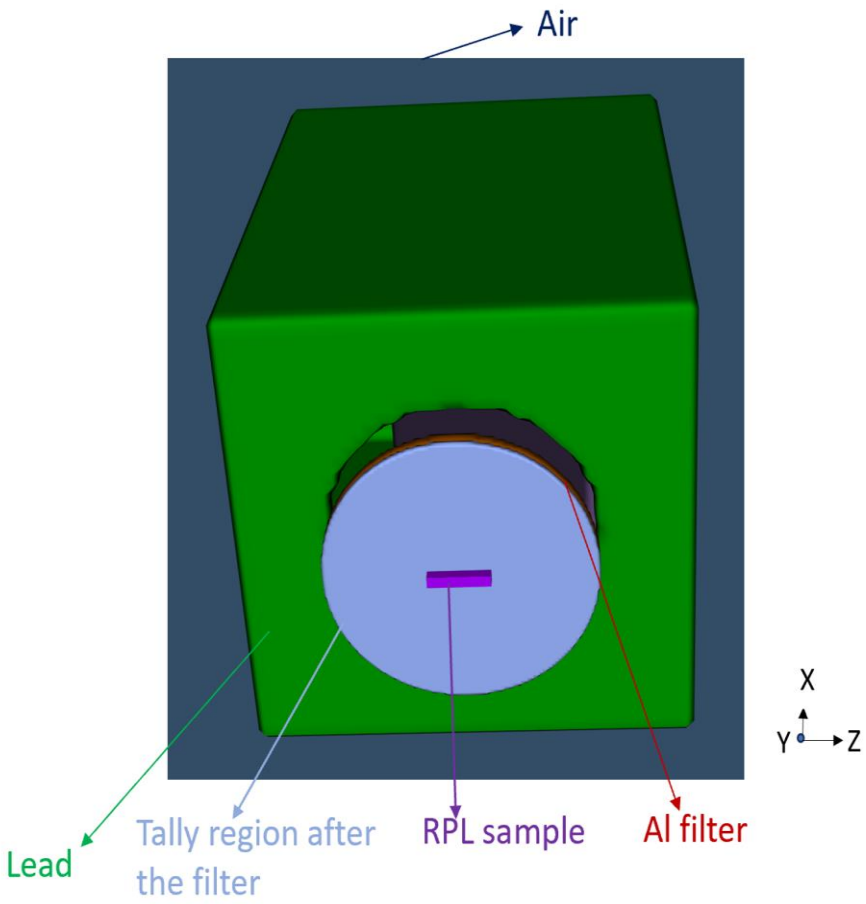

Figure 13: 3D view of the simulation setup.

2.5 Simplified Model of the Dosimetry Simulation Setup

In a third set of simulations, the model has been further simplified using a pencil beam, polychromatic energy photon source and the directivity is also set towards Z-axis. The aim of this simplified model is not to replicate the facility with accuracy, but to compare different irradiation conditions (for example, with and without shielding) and with different types of filters to compare their effectiveness. Additionally, a pencil beam photon sources can allow relatively shorter CPU computational time to be achieved in comparison to anisotropic photon sources with a similar number of primary photons. As shown in the schematics in Figure 15, the center of the dosimeter and other samples are positioned at the coordinate point (0,0,8) which is located 8 cm far from the source (0,0,0) and different thickness of filters made of Cu and Al are also used just 3 cm far from the photon source. The sample is partitioned in to slabs with an resolution of 0.1 mm in z-axis direction.

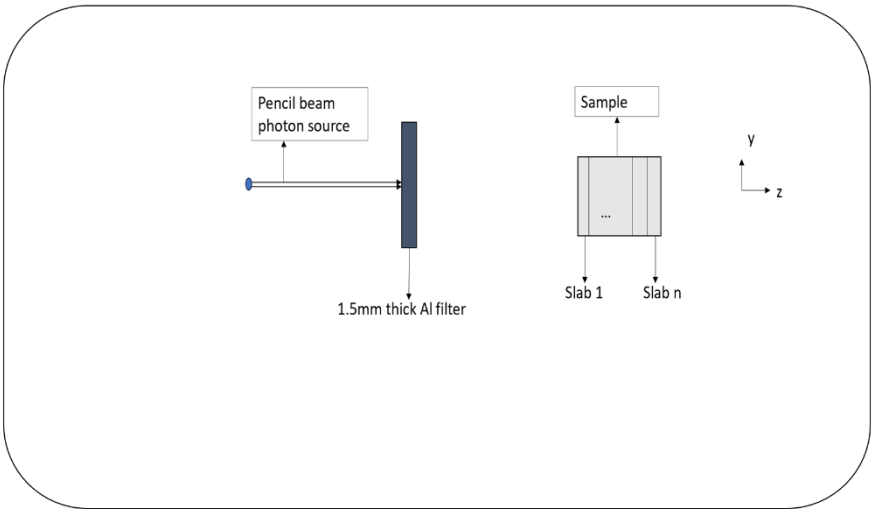

Figure 14: Simplified model of the RPL dosimetry simulation schematics in PHITS. All the dimensions used are not in the right scale.

PHITS 3D viewer which is a viewer system provided by PHITS and allowing the realised geometries to be visualized. In Figure 15, realized with PHITS 3D viewer, a 1.5 mm Al filter is shown in brown colour and a cylindrical tally region in blue colour. The blue colour in this case indicates that the filter and sample both are situated in air, as the viewer associate colours to specific materials. In this set of simulations, different types and thickness of filters are introduced to study their impact on the energy spectrum and on the dosimetry in the samples. The center position of the filter, tally region, and sample are aligned.

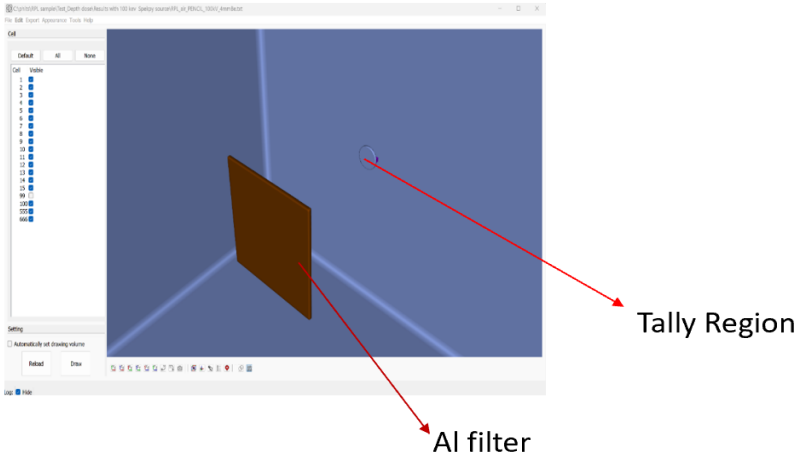

Figure 15: PHITS 3D view for the simplified model of the dosimetry simulation setup.

Chapter 3

Results and Discussion

In this section results such as X-ray spectra characterizations, dose deposition in different sample under different simulation conditions, effect of the position of the filter on samples dose deposition, effect of different filters on the sample dose distributions and calibration factor determination ways are presented and discussed.

3.1 X-ray Spectra Characterization

In this section, the following simulation results are analyzed.

- X-ray spectra (photon fluence per square centimeter per primary electrons as a function of photon energy) before and after the Be exit window in PHITS
- Photon fluence spectra comparisons between SpekPy and PHITS after Be filter
- Photon fluence as a function of photon energy with and without Al as an additional second layer filter
- Particle trajectories per square centimeter per primary electrons in xz -plane to have an overview of the photon emission and the relative statistical error map distribution in the modelled X-ray tube

Most of the quantities here reported are expressed per primary particles (electrons or photons, depending on the used sources), so the reported results are for the moment used for comparisons only. For example, relative comparisons showing the effect of different filters on the X-ray spectra are discussed. In all the reported simulations the statistical error is lower than 6%.

3.1.1 Effect of the Be filter

In Figure 16 a), the X-ray spectra have been simulated using PHITS with an electron pencil source, as described in Section 2.3. The results show the photon fluence, expressed in cm^{-2} /primary electron) as a function of the photon energy for an energy range from 0 MeV to 0.1 MeV, using an energy bin resolution of 0.5 keV. Tungsten characteristic emissions, corresponding to discrete peaks at 58.8, 67.7, 8.4, 9, and 11.3 keV for its X-ray characteristic lines K_α, K_β, L_α, L_β, L_γ respectively are visible. The overall spectrum results from two contributions, that are clearly visible in the graph; the bremsstrahlung contribution that is continuous and whose photon energy maximum correspond to the maximum voltage, and the characteristic peaks, which have the typical energies corresponding to W. So, for 100 keV electron source, the maximum photon energy is 100 keV. As expected, the photon fluence is higher for the low energy photons. The positions of the characteristic peaks, the maximum energy and the qualitative shape of the fluence spectrum are all in agreement with the literature [7], [30].

Electron transport is a computationally intensive process due to the highly interactive nature of these particles with matter. As a consequence, techniques are employed to reduce the CPU computational time, such as shared memory parallelization and cell importance variance reduction techniques. In these conditions, 5-day long simulations

were necessary to collect spectra with relative statistic errors lower than 6 % in all the energy bins. In most energy ranges however the error was limited to a maximum of 3%.

Two different spectra are compared in Figure 16 a): the photon energy spectrum produced by the target and computed in a reference position (in blue) and the same spectrum filtered by a 4 mm thick Be layer, replicating the real configuration of the X-ray tube, computed in a different reference position located after the filter. The comparison between the two spectra demonstrates the effect of Be as a first filter on the X-ray spectra. The Be window is used to filter out the lower part of the photon energy spectrum. Photons with energy lower than approximately 3.5 keV are attenuated by 3 orders of magnitude from the ones before Be filter.

The spectra simulated by PHITS are then compared with a spectrum provided by SpekPy in similar conditions (100 kV tube potential, tungsten with 30 degree target angle and 50 degree emission angle, 4mm thick Be filter). As shown in Figure 16 b, photon fluence after the Be filter simulated by PHITS is actually per primary. The spectrum is normalized using a constant value to be able to to compare it directly with the one generated by To realise the comparison, the PHITS spectrum is shifted so that the bremsstrahlung contribution of the two spectra overlaps. The result shows a good qualitative agreement for the Bremsstrahlung component, but the characteristic X-ray spectrum, especially for photons that have energy in the range between 8 keV to 9 keV appears to be underestimated by PHITS in comparison to Spekpy. The ratio in the photon fluence peaks in SpekPy to PHITS can reach a factor of 10 for the lower energy characteristic peak at around 8.4 keV. By contrast, a better agreement is achieved for the characteristic peaks positioned at higher energies. For example, The origin of this difference is at the moment unclear. As possible hypotheses, it could be attributed to the differences between the real X-ray tube configuration and the simplified model realized in PHITS. For example, the size and the exact geometry of the anode target in a commercial X-ray tube is not precisely known due to confidentiality information. The differences between the X-ray spectrum simulated by PHITS and the one produced by Spekpy need to be systematically analyzed, and this will be the focus of future investigations.

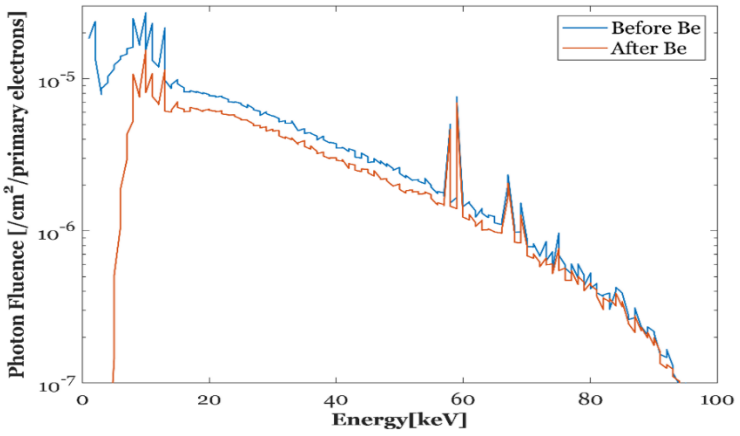

a)

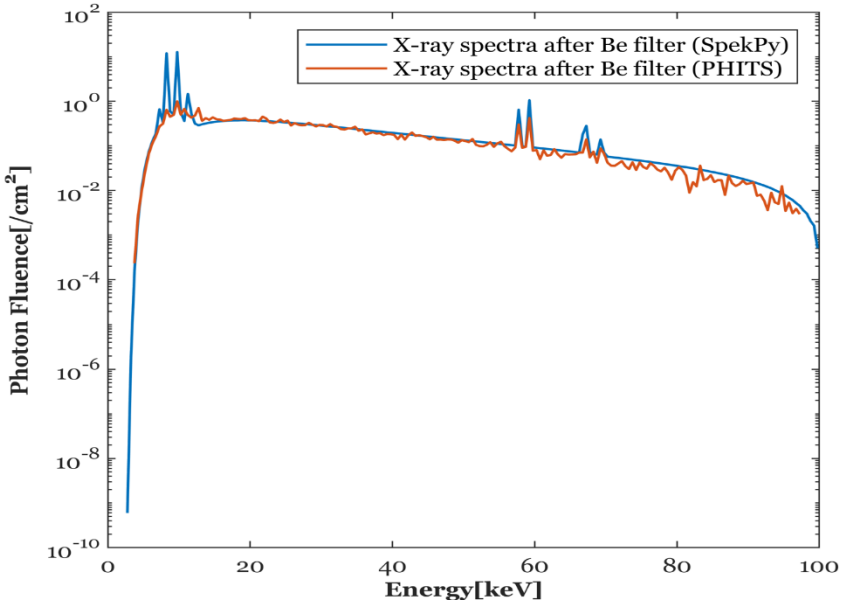

b)

Figure 16: X-ray spectra simulated in PHITS and SpekPy: a) Effect of Be window or filter on the X-ray spectra (the spectra simulated with PHITS before and after Be filter), b) The X-ray spectra after the Be filter simulated in SpekPy and PHITS.

3.1.2 Effect of 1.5 mm Al shielding

Figure 17 shows the effect of an additional 1.5 mm thick Al filter on the X-ray spectra for the case of an isotropic photon source as described in Section 2.4. In this case, the photons exiting the Be window are shielded by a second Al layer, resulting in a remarkable spectrum hardening. Photon fluence with photon energy lower than approximately 10 keV are strongly attenuated by five orders of magnitude from the fluence without Al filter. At 20 keV, at least about one order of magnitude in fluence is attenuated with the use of the filter. So, the use of filter makes the X-ray spectrum harder, meaning that its average energy increases. In the frame of this work, filters are used aiming at having photons with higher energies, or more specifically to cut low energy photons that would deposit dose in a highly inhomogeneous way in the samples of interest. The spectrum hardening is functional to the desired homogeneity in this case.

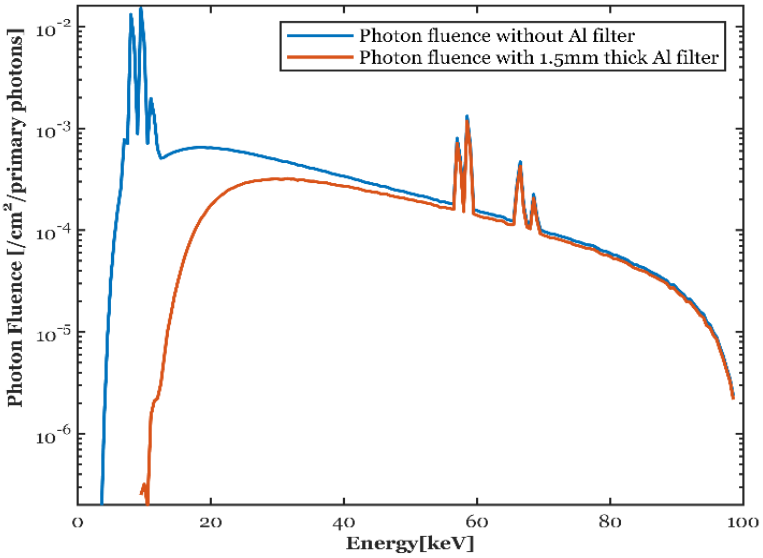

Figure 17: Effect of 1.5 mm thick Al filter on X-ray spectrum.

3.1.3 Particle Trajectories and Statistical Error

PHITS provides as output a map of the simulated particle trajectories and the associated statistical error map. Figures 18 a) and b) show a typical PHITS particle trajectory plot and the relative statistical error for the modelled X-ray tube geometry respectively. As expected, the particle fluence is higher near the source, which is located at the origin of the coordinates, and in the direction of photon emission. The statistical error correspondingly increases in the areas of the geometry where fewer particles are transported, specifically, on the opposite side of the emission path and increasing the distance from the source. The used model allows good fluence statistics to be reached in the areas of interest which is below the X-ray source, where the samples are placed and irradiated. In fact, the overall statistical error on the fluence in that position is lower than 0.01 (corresponding to the green area in Figure 18 b), which normally considered as a very satisfactory values in Monte Carlo simulations.

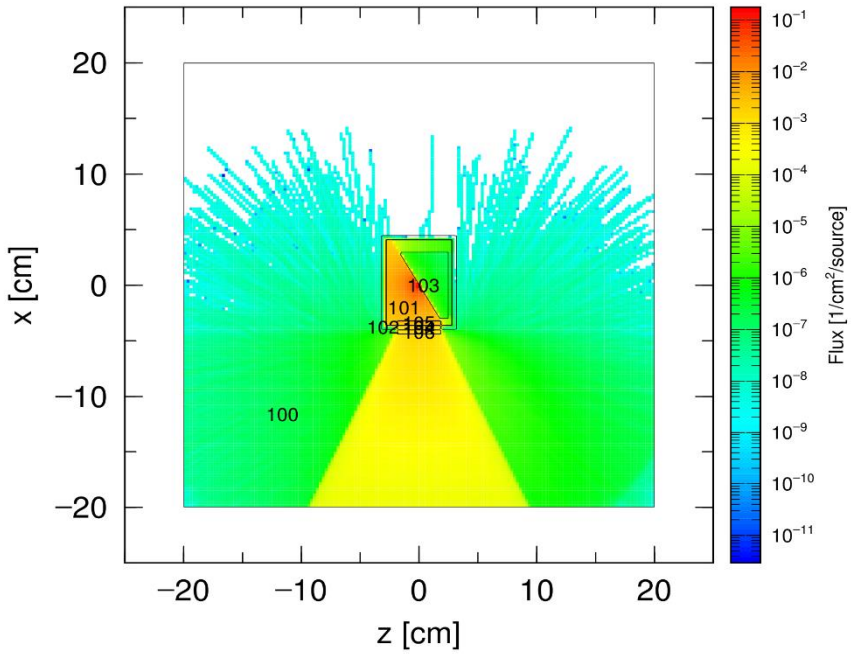

a)

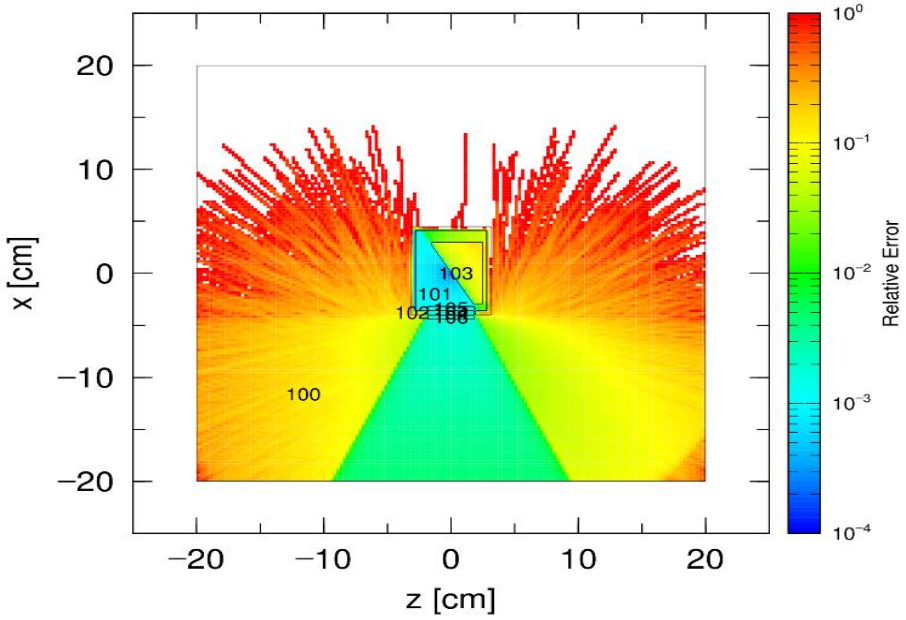

b)

Figure 18: Particle trajectories and statistical error map produced by PHITS.

a) Particle trajectories(electrons and photons) for the designed X-ray generator models in xz plane, b) Relative statistical error maps for the modelled X-ray tube in the same geometry.

3.2 Absorbed Dose Estimation in RPL and Water Samples

The spectra collected in different conditions are used to evaluate dosimetry in the configurations presented in Section 2.4, aiming at achieving a satisfactory dose homogeneity in macroscopic samples. Using an isotropic point photon source and a 5 cm source-sample spacing distance, the relative dose distribution as a function of the sample depth compared in different cases, in particular:

- Dose in the RPL sample with and without the use of a 1.5 mm thick Al filter is compared in Figure 19.
- Dose distribution in the RPL sample in the X-ray spectrum generated at 100 kV and 160 kV tube voltages is compared by keeping 1 mm thick Al filter in both conditions, as reported in Figure 20.
- Dose deposited in the RPL sample and in an equivalent volume of water in the same simulation conditions, filter thickness, and corresponding to spectrum at 100 kV tube potential is compared. The dose deposited in the sample made of water is used as a reference.

Results in these configurations are reported in Figures 19, 20 and 21, respectively. Details are provided in the following sections.

3.2.1 Effect of 1.5 mm thick Al filter in RPL Dose Deposition

In this section, the term 'unshielded' is referred to simulations in which only 4 mm thick Be window, already incorporated in the X-ray tube, is present, while 'shielded' is referred to configurations including additional Al filters of different thicknesses. As shown in Figure 19, for the unshielded configuration, the dose in RPL dosimeters decreases sharply as a function of the sample thickness, from the top slab to the bottom slab. This sharp dose reduction along the sample depth is also in agreement with previous studies for phosphate based glasses [3]. As already mentioned in section 2.4, the sample is divided along its depth into 15 identical slabs with 0.1 mm resolutions. As expected, the highest dose is delivered to the slab close to its top surface. Then the dose drastically decreases as the photon beam attenuates inside the sample. The dose in the top slab is approximately 20 times higher than the dose in the bottom slab.

By contrast, in the shielded case, as it is previously mentioned, the lower energy portion of the X-ray spectra is filtered out by the Al filter, as shown in Figure 17. The dose contribution of these low-energy photons (for example, up to approximately 20 keV) seems to be the ones mostly contributing to the total deposited dose, at least in the first 0.5 mm of the RPL material. In fact, when they are cut by the Al shielding, the dose gets more uniform and accordingly it can be assumed that these low energy photons are responsible for the highest dose inhomogeneities in the sample volume. The deposited dose value variations in the sample layers or slabs can be also assessed by a depth dose uniformity ratio (DUR) [31], [32], calculated using the following equation:

$$\mathrm{DUR} = \frac{\text{Maximum dose}}{\text{Minimum Dose}} \tag{10}$$

The dose as a function of the depth for the RPL dosimeter becomes much more uniform as compared to the unshielded case, and the DUR as calculated using equation (10) correspondingly decreases from 18.33 to 1.66. This improvement can be considered as satisfactory and allows irradiation of dosimeters in these conditions to be performed.

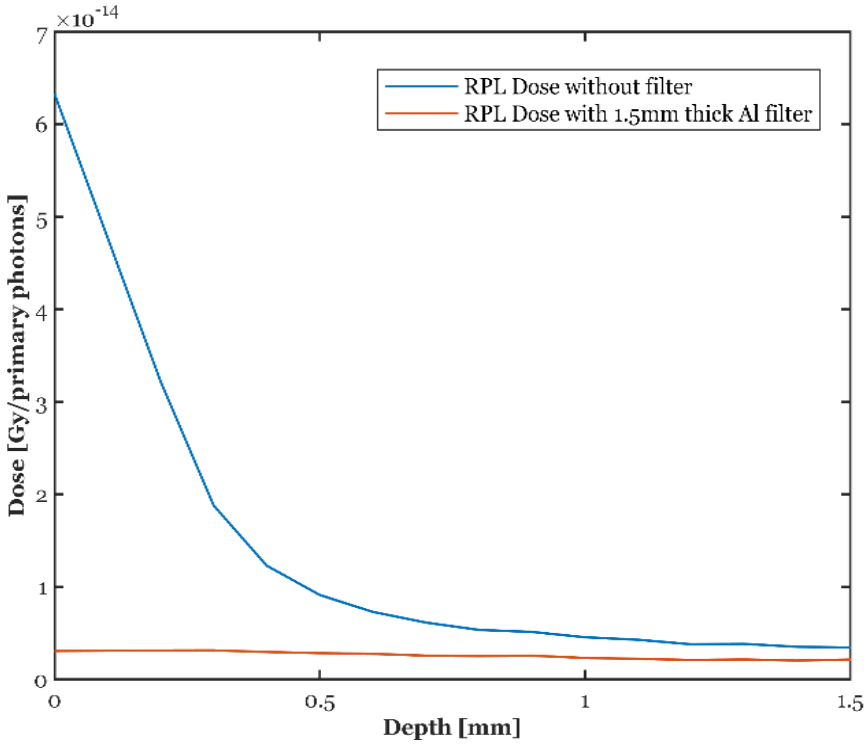

Figure 19: Deposited Dose in RPL without and with filter.

3.2.2 Effect of X-ray Tube Potential on RPL Dose Deposition

The spectra used to realize the different photon sources used in this Section are obtained using Spekpy. The comparisons between doses are done in all cases per primary photons. As shown in Figure 20, the deposited dose across the sample depth with the shielded configuration at 160 kV X-ray spectra is 22 % higher than the dose deposited at 100 kV, this is due to an increase in the mean energy of the X-ray irradiator at 160 kV tube potential. The bremsstrahlung component of the X-ray spectrum energy ranges up to the maximum photon energy. So, 160 kV and 100 kV tube potential mean that we have photons up to 160 keV and 100 keV, respectively. The dose gradient along the RPL sample depth at these two tube voltages with the use of 1 mm Al filter in both cases shows only minor differences. The depth dose uniformity ratio is 1.66 and 1.62 at 100 kV and 160 kV tube potentials respectively. This indicates that it is better to use 160 kV tube potential than 100 kV tube potential in the case where an Al shielding is used if it is really needed to achieve a relatively higher dose rate in parallel with a good absorbed. dose homogeneity for RPL sample in irradiation experiments with this type of tube.

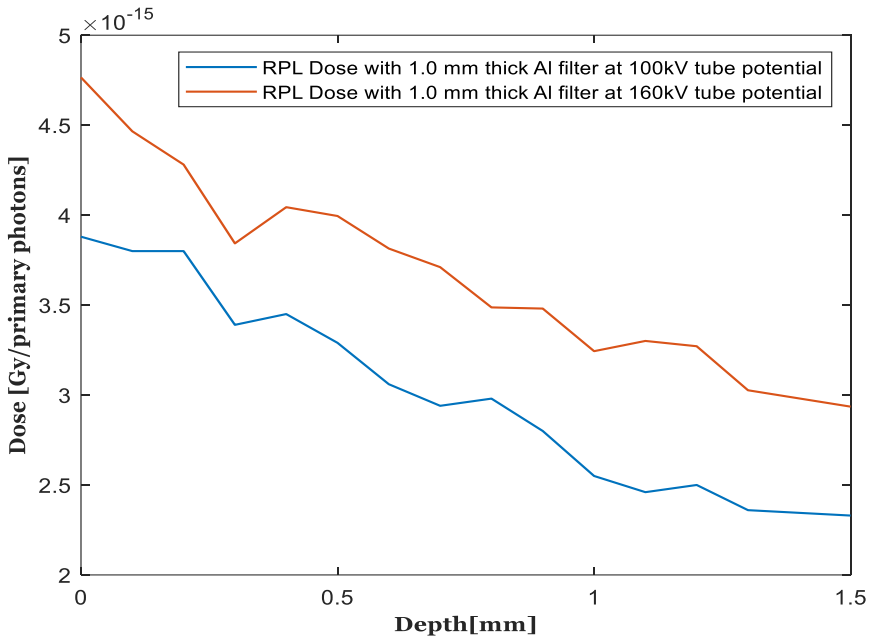

Figure 20: RPL deposited dose at 100 kV and 160 kV X-ray tube as a function of the RPL sample depth.

3.2.3 Absorbed Dose Comparisons in RPL and Water

The absorbed dose comparisons for water and RPL is simulated under the same conditions described in section 3.2.1. A 1.5 mm thick Al filter and spectrum generated at 100 kV are used. Figure 21 shows a comparison between the dose absorbed by the RPL dosimeter and the dose absorbed by an identical volume of water equally divided in identical slabs with a resolution of 0.1 mm. The average dose absorbed by the RPL sample is roughly 3.73 times higher than the absorbed dose in water. This comparison can be useful to calculate the calibration factors for the deposited dose in the sample using water as a reference. Doses are often expressed in Gy in water, especially the ones from calibration measurements. So, estimation of a calibration factor to convert a dose in water to the absorbed dose in any medium (RPL in this case) is really necessary.

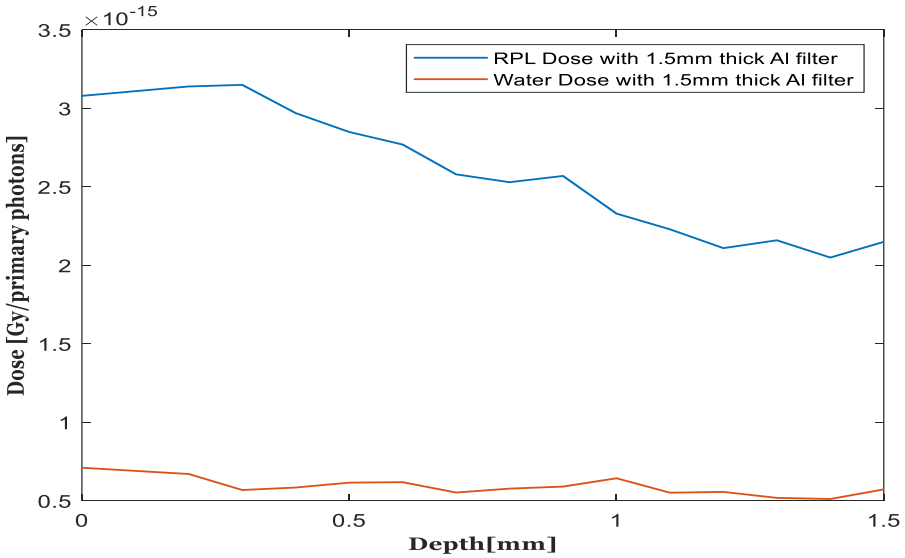

Figure 21: Deposited dose comparison in RPL and water.

The determination of the calibration factor allowing the dose in water to be converted in the dose absorbed by the RPL dosimeter is further discussed in Section 3.6. The absorbed dose along the sample depth for water sample is uniform and the DUR is about 1.25 only, while for the RPL sample it is much higher. The dose uniformity ratio and average dose for the RPL samples at different tube potentials and Al filter thickness are reported in Table 4.

	Dose Uniforimity Ratio (DUR)		**Average Dose (Gy/ primary photons)**	
	100 kV	**160 kV**	**100 kV**	**160 kV**
Without filter	18.33	12.2	1.22e-14	1.05e-14
1 mm thick Al	1.66	1.62	3.04e-15	3.71e-15
1.5 mm thick Al	1.43	1.4	2.58e-15	3.3e-15

Table 4: RPL Dosimeters Dose Uniformity Ratio and average dose in Different Conditions.

The average dose for the RPL sample with the use of 1 mm or 1.5 mm thick Al filter is 10 % of the average dose in the unshielded case. For the cases when the filter is used, the dose at 160 kV is 21 % higher than the dose at 100 kV tube potential.

Furthermore, the average dose for the exact cylindrical shape RPL sample has also been simulated to evaluate the validity of shape approximation in dose distribution assessment. There was only a 2% difference in the average dose value of the sample with cylindrical slabs and rectangular slabs of the RPL sample. So, the two values are compatible within the statistical error. This helps us to use the approximate rectangular geometry slabs of the sample for most of our simulation.

3.3 Effect of Filter Position on Macroscopic Samples

A different geometry was implemented, in which the position of the source and of the sample is kept constant, while the position of the shielding is moved, to evaluate possible effects of the shielding position on the dose. The shielding was moved from a maximum of 6 cm to the sample to a limit position where it is in contact with the sample. The photon source used in this and in the following results is a pencil beam photon source, as described in section 2.5. The effect of the position of a 1.5 mm thick Al filter on the dose deposition across the sample depth is presented in Subsections 3.3.1 and 3.3.2. A sample-to-filter spacing distance of 6 cm, 3 cm, and 0 cm (with the filter directly in contact with the top of the sample) is used for the investigation of the study. All the other simulation conditions are kept identical.

3.3.1 Effect of Al filter Position on Sample Dose Deposition

Simulations were performed for different types of samples starting from RPL, and then silica and water. The dose attenuation with the sample depth is simulated in PHITS with a 1.5 mm thick Al filter and different sample-to-filter spacing distances.

Based on the results of the simulations shown in Figure 22 a), it can be observed that, as expected, a variation of a few centimeters, ranging from 3 cm to 6 cm, in the spacing between samples and an Al filter does not affect significantly the dose distribution in the samples. The dose in RPL sample with 3 cm and 6 cm gap between the sample and the filter are in fact overlapped. It is also important to note that the air act as a shielding, exactly like aluminium or beryllium or any other material, but since its density is about three orders of magnitude lower, the attenuation is also much lower. In these simulations, the distance between the source and the sample is kept constant. So, the shielding effect of the air also remains approximately the same, because the photons have to cross the same thickness of air in all the configurations. What changes is only the relative position of the shielding in comparison to the sample, and this can lead to interface effects when the shielding is directly in contact with the sample. However, if the spacing distance is high enough, the primary photon beam can undergo attenuation. As the sample is moved farther away from the beam or particle source, there could be a reduction in the intensity of the photon beam and this in turn can lead to a reduction of the absorbed dose as seen in Figure 18a. Such kind of simulations provide insights into predicting experimental uncertainties that may arise during irradiation experiments and can help also mitigate concerns about uncertainties in the filter or shielding positioning during irradiation campaign experimental setups.

The production of secondary electrons resulting from the interaction between primary photons and different samples such as water which is used as standard reference dosimetry, RPL, and silica contributes to the dose distribution. All the samples are exposed to the same photon spectrum (except for the spectrum variation and attenuation due to the interactions with the sample itself) but, the materials are different so the attenuation of the primary beam and the production of all the secondaries (electrons and photons) correspondingly changes.

In the same photon energy spectrum as shown in Figure 22 b), the RPL sample absorbs the highest amount of dose, followed by silica which is used for a comparison study. Additionally, DUR along the sample depth is about 1.6. In contrast, the dose in the top and bottom slabs of the water sample is nearly identical, resulting in a more uniform dose distribution along its depth and its DUR is 1.2. When a shielding is utilized directly on top of the samples without any spacing, there is an additional dose contribution as shown in Figure 22 b). This slight increase in dose when the filter is directly attached on top of the samples might be due to the secondary electrons produced in the shielding material and entering the following sample, giving an additional contribution to the dose. This effect can be attributed to the interface between different materials, and accordingly, as it is previously mentioned, it is particularly significant in the top slabs or layers near the surface of the samples.

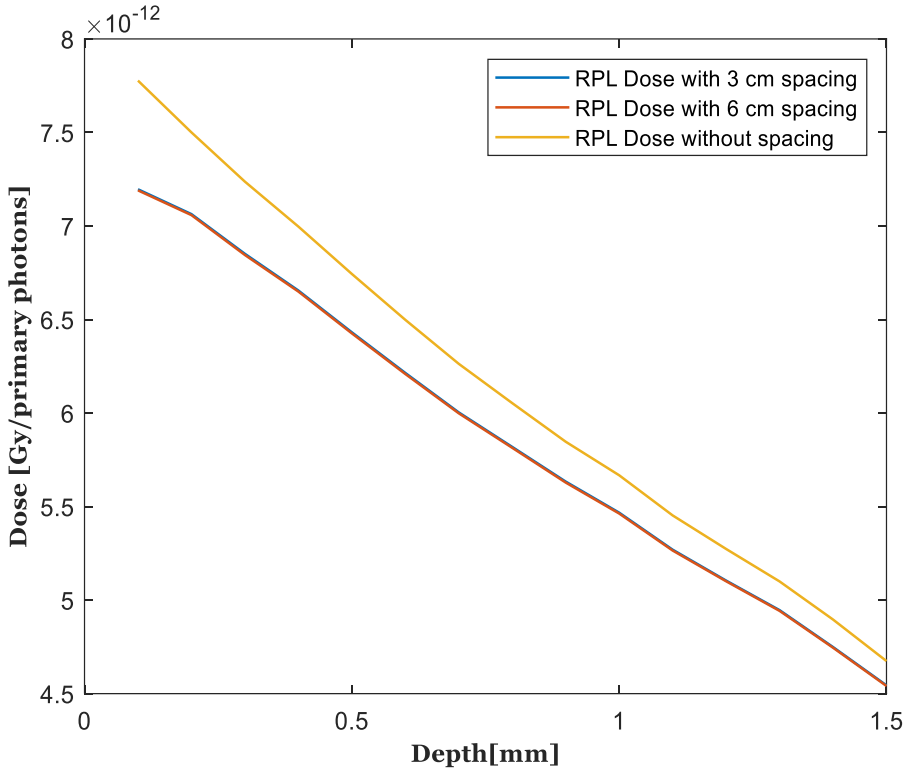

a)

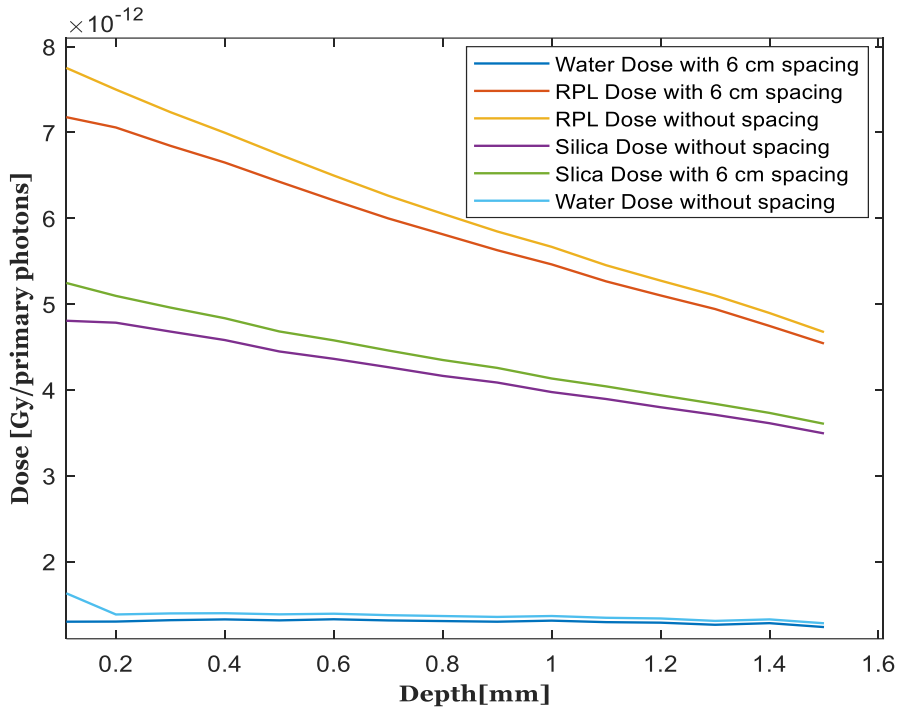

b)

Figure 22: Effect of Al Filter Position on the Dose Deposition Across Samples Depth.

a) Effect of Al filter position on the dose distribution in RPL sample , b) Effect of Al filter position on different materials such as silica, RPL, and water with 0.1 mm slab resolution for all the samples.

Also, with this type of configuration with pencil beam photon source, the deposited dose gradient along RPL sample depth is also visualized using a dose mesh. The sample is positioned at a coordinate point (0,0,8), 8 cm far from the source (0,0,0) and the sample thickness is from z= 8 cm to z= 8.15 cm. The X-ray photons sources are directed along the z-axis and are perpendicular to the sample. There is a significant deposited dose gradient along the RPL sample depth in the case of unshielded configurations as shown in Figure 23 a). For the shielded configuration which is shown in Figure 23 b, the homogeneity is much better than the unshielded one. The maximum dose in the unshielded configuration is about roughly 20 times the deposited dose in the last layer of the sample (DUR=20). But, for the shielded case the maximum and minimum dose is about a factor of 2. As per the previous case, a higher dose is deposited in the first layers of the sample.

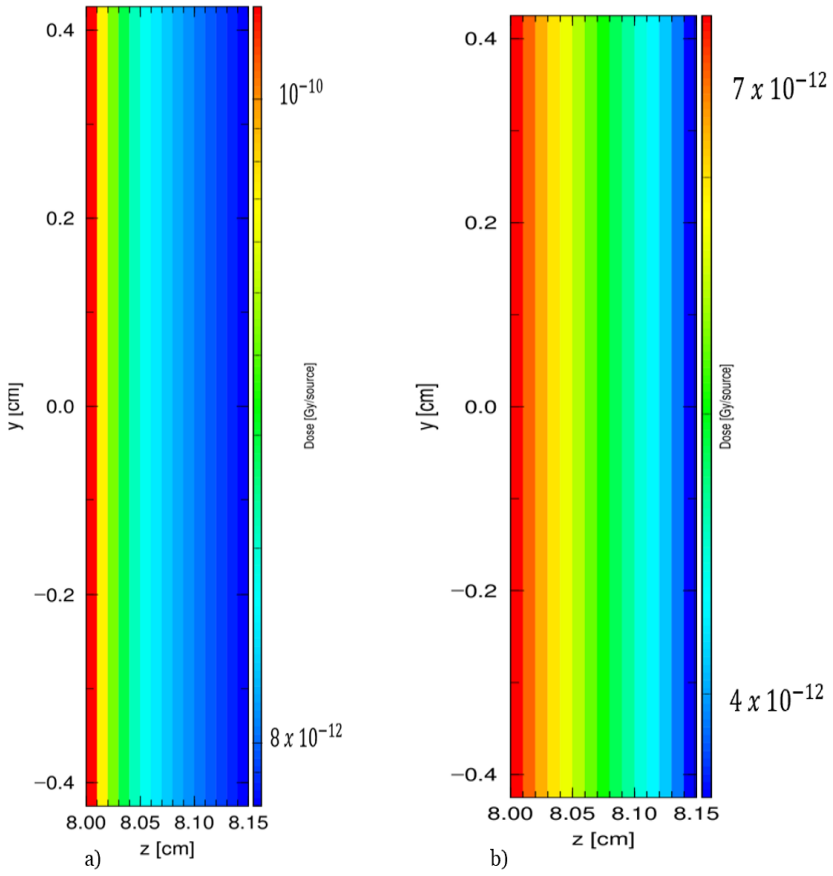

Figure 23: Dose distribution gradient with and without filter.

a) without filter , b) with the use of Al filter. The scale in the two graphs is different.

Dose inhomogeneity can be defined as the percentage difference between the maximum dose or minimum dose and the average dose of the dosimeters and samples, and it is higher for the RPL dosimeters in comparison to water. The dose inhomogeneity for the RPL dosimeters, silica, and water in different position of the filter is presented in the Table 5. The inhomogeneities are exacerbated when the shielding is placed in direct contact with the sample, because this gives extra dose contribution to the slabs corresponding to the maximum dose already.

	Inhomogeneity (%)	
Sample	filter - sample spacing (6cm)	sample - filter spacing(0 cm)
Water	± 4	± 19
Silica	± 15	± 20
RPL dosimeters	± 30	± 38

Table 5 : Dose Inhomogeneity Calculations for Different Samples.

The estimated absorbed dose in water and RPL can be used to determine the calibration factor used to estimate the absorbed dose in RPL dosimeters starting from a dose in water, as detailed in Section 3.6.

3.4 Deposited Dose in Samples with 10 μm Slab Resolution

In the same simulation condition as Section 3.3, an attempt was performed to calculated the deposited dose in RPL and water in 10μm thick slabs, aiming at achieving a better spatial resolution. Result is reported in Figure 24. A noticeable build-up region is observed, corresponding to an initial region where the absorbed dose is increased as the sample depth increases. The results are compatible with the ones previously collected with depth spatial resolution of 0.1mm. But, unlike the simulations with 0.1 mm slab resolution, simulations with 10 μm slab resolution takes 4 to 5 hour of CPU computational time and the relative statistical error in this case is 5%. But, in simulations with 0.1 mm slab resolution, the error is less than 3% and can take about 2 hours with appropriate variance reduction techniques to reduce the computational time.

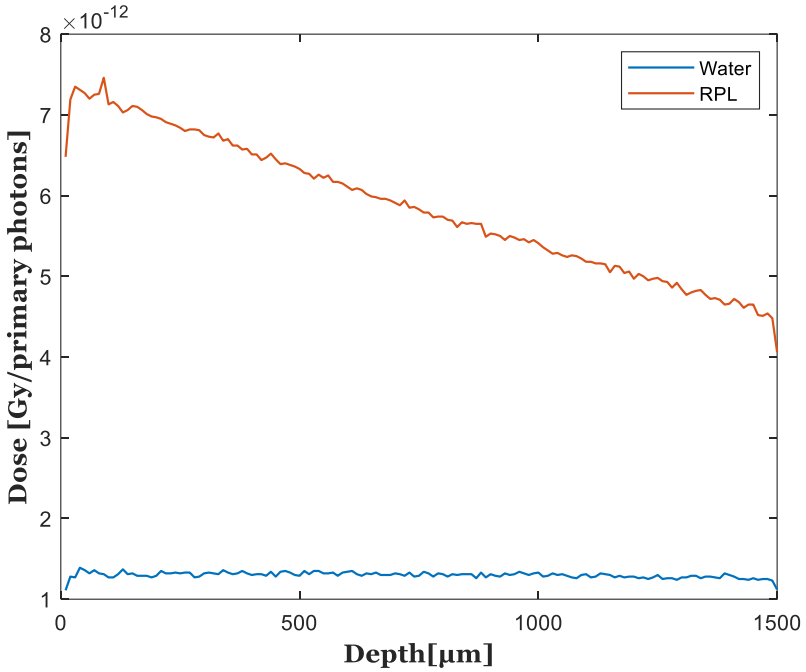

Figure 24: Deposited dose in RPL and water with 10µm slab resolution.

3.5 Effect of Different Types of Filters on Deposited Dose in RPL Glass

Before we see the effect of the filter on dose deposition, it is better to see first how the effect of the different types of filters such as Al and Cu on the X-ray spectrum looks like by simulating the X-ray spectra after the filters in PHITS. All the simulation conditions are the same as described in Section 3.3. As shown in Figure 25 a), with the use of Al filters with thicknesses (1 mm, 1.5 mm, and 3 mm), it is possible to effectively attenuate the fluence by three orders of magnitude from the maximum photon fluence. Photons with energies less than about 10 keV (for 1.5mm and 1 mm thick Al filters and 15 keV in the case of 3 mm thick Al filter are therefore highly attenuated. In comparison to Al, Cu filters of similar thickness attenuate a higher portion of the low-energy spectrum, particularly concerning photons having energies lower than roughly 36 keV can be filtered out with such kinds of filters. The spectrum becomes much harder in the case of Cu filters than in the case of Al filters. The dose inhomogeneity in RPL dosimeters can be reduced to less than 15 % and 8% with the use of 3 mm thick Al filter and 1.5 mm thick Cu filters, respectively. As shown in Figure 25 b) the deposited dose gradient along the RPL sample depth reduces as the Al filter thickness increases. But also, the average dose in the RPL sample with the use of 3 mm thick Al and a 1.5 mm thick Cu filter is reduced by almost 35% and 95 % respectively of the average dose with the use of a 1.5 mm thick Al filter. A compromise is necessary between achieving satisfactory dose rates and satisfactory dose homogeneity. Here a 1.5 mm thick Al filter is used as a reference for the comparison as this filter was used in the experimental irradiation campaigns.

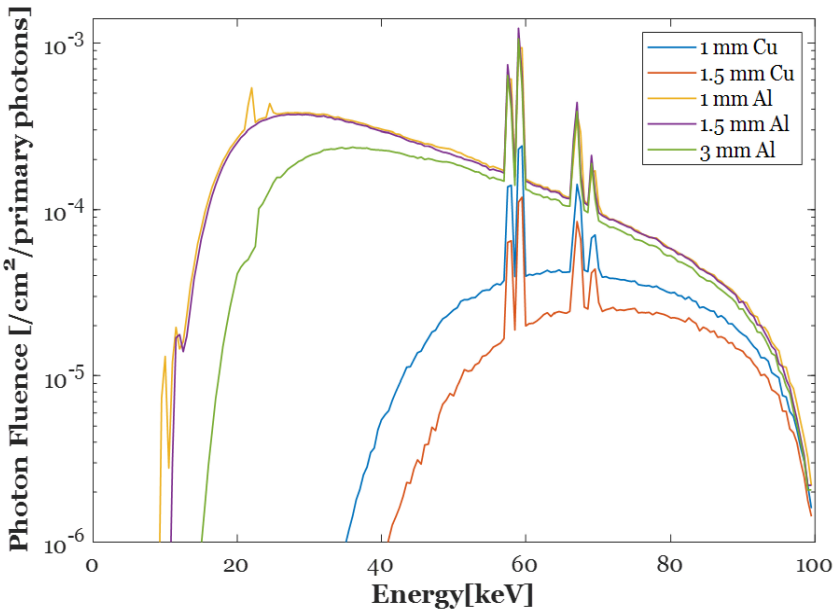

a)

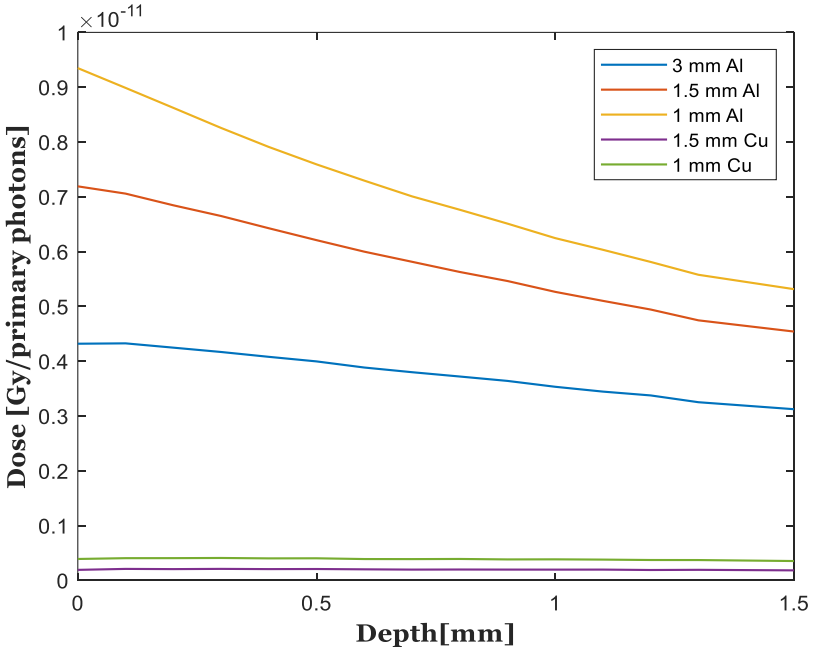

b)

Figure 25: Effects of different filters on the X-ray spectrum and on RPL deposited dose.

*a) E*ffect of different filters on the X-ray spectrum (log scale), and b) *E*ffect of different filters on RPL deposited dose.

3.6 Estimation of Absorbed Dose Calibration Factor in RPL Dosimeters

The work reported in this Section was accomplished in collaboration with CERN's *Radiation to Electronics* project. The simulations, irradiations and the absorbed dose calculations were done in UJM as part of the present work, while the dosimeter readout was performed at CERN following the methodology described in [25]. The methodology and the collected results are reported in a contribution submitted and accepted to RADECS 2023 Conference [33] and are currently in preparation for publication.

Four RPL samples were irradiated at a constant dose rate in water ($\dot{D}_w$ = 0.58 Gy[H20]/s) with irradiation times, corresponding to 10 min (D1 sample), 100 min (D2), 10 h (D3) and 60 h (D4). Four additional RPL samples (namely, R1, R2, R3 ,and R4) with different dose rates ranging from 0.47 Gy[H20]/s (R1) to 0.047 Gy[H20]/s at the same target dose in water (Dw = 3.04 kGy[H20] for R4) were irradiated. Measured total absorbed doses in RPL, denoted by ($D_{RPL(Meas)}$) for the whole 8 samples are shown in Table 6, along with the values of $\dot{D}_w$ and the measured dose in water denoted by ($D_{w(Meas)}$) for the two irradiation campaigns. The dose rate was measured with a commercial ionization chamber, produced by PTW model no. 23344 [34]. The chamber provides a dose rate in water at equilibrium conditions. It is denoted by $\dot{D}_w$ and expressed in Gy[H20]/s. Total doses in water for the duration of each dosimeter irradiation T_{irr} can be calculated using the following equation (11):

$$D_{w\,(Meas)} = \dot{D}_w \cdot T_{irr} \tag{11}$$

The sample to source distance was around 8 cm. A 1.5 mm thick aluminium filter was placed between the source and the sample, at about 3 cm distance from the sample in order to improve dose homogeneity based on the simulation outcomes discussed in Section 3.2..3.

The simulations in water are used to mimic the readout ionization chamber and to compute a factor to convert $D_{w(Meas)}$ to the average dose deposited by the RPL dosimeter, referred to as $D_{RPL\,(calc)}$ using the following equation (12):

$$D_{RPL\,(Calc)} = D_{w\,(Meas)}\, K_{sim} \tag{12}$$

where the simulate conversion factor K_{sim} is:

$$K_{sim} = \frac{D_{avg,RPL(sim)}}{D_{w\,(sim)}} \tag{13}$$

$D_{avg,RPL(sim)}$ is the simulated average dose in RPL sample and $D_{w\,(sim)}$ is the simulated dose at the equilibrium in an identical volume of water, in the shielded configuration, as indicated in Figure 21. Using Equation (13), a K_{sim} value of 3.7 is found in this irradiation conditions. The calculated and the measured absorbed doses are presented in Table 6.

Samples	$\dot{D}_w$ Gy[H2O]/s	$D_{RPL\ (Calc)}$ kGy[RPL]	$D_{RPL(Meas)}$ kGy[RPL]
D1	0.58	1.29	1.0
D2	0.58	12.88	12
D3	0.58	77.26	85.9
D4	0.58	463.54	416.9
R1	0.47	11.25	10.9
R2	0.19	11.25	12.6
R3	0.09	11.25	10.7
R4	0.047	11.25	11.1

Table 6 : Summary of Irradiation Campaigns for the RPL Dosimeters.

The calculated and measured absorbed dose errors are 30 % and 5 % respectively. The calculated absorbed dose in the RPL dosimeters is in good agreement with the experimentally measured absorbed doses as shown in Figure 26 and Figure 27 for the two sets of dosimeters. This represents a validation of the realized simulation models in the analyzed configuration and for the irradiation of RPL dosimeters.

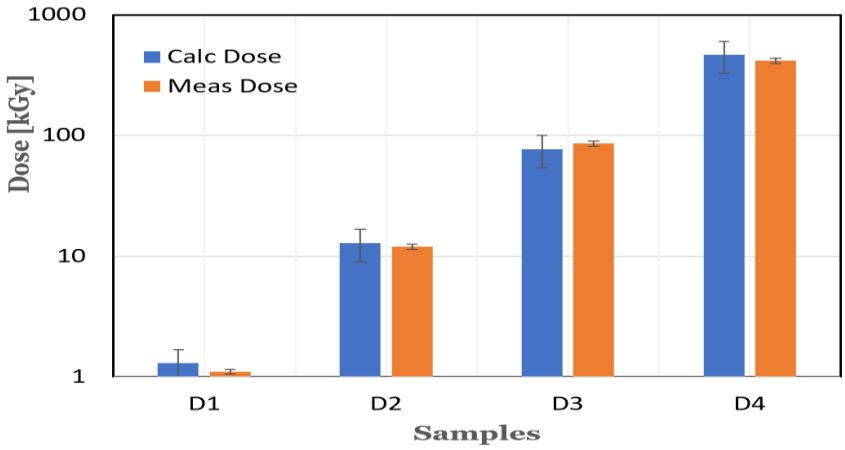

Figure 26: Calculated (Calc) and Measured (Meas) absorbed doses in RPL samples D1, D2, D3 and D4.

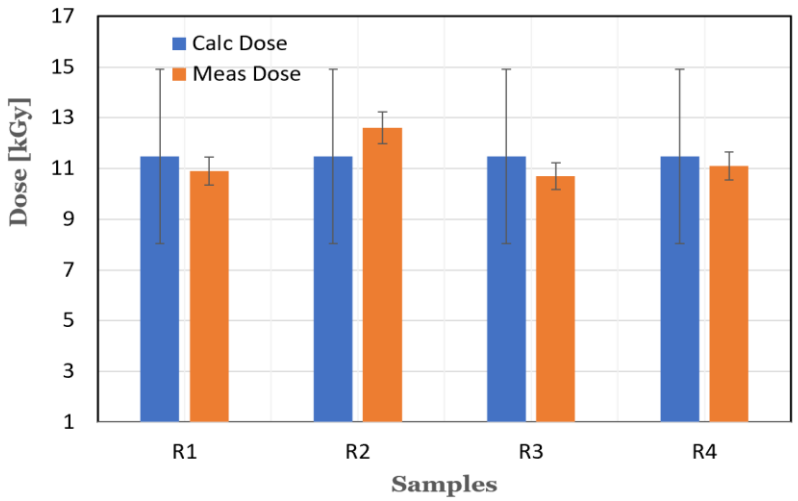

Figure 27: Calculated (Calc) and Measured (Meas) absorbed doses in RPL samples R1, R2, R3 and R4.

As shown from in Figure 27, the error bars for the calculated dose is a bit higher. This is due to the dose inhomogeneity along the sample depth. This inhomogeneity can be further improved to 8 % with the use of 1.5 mm thick Cu filter as discussed in Section 3.5.

Chapter 4

Conclusions and Future Works

4.1 Summary and Conclusions

In the present study, a model of the X-ray irradiation facility has been successfully realized with the Monte Carlo code PHITS. The spectra produced by a commercial X-ray tube were simulated and used to study the feasibility of irradiations of macroscopic samples. Simulations show that the utilization of a Be exit window as a primary filter and different thicknesses of Al as a secondary filter, can effectively attenuate X-ray spectra's lower energy photons up to energies roughly corresponding to 3.5 keV and 10 keV, respectively. These low-energy photons are responsible for a considerable contribution to the dose deposition in macroscopic samples such as RPL dosimeters, and the same apply to different materials such as silica, causing high dose inhomogeneity across the dosimeter volume, since the dose is mostly deposited in top layers. Accordingly, 1.5 mm, 3 mm thick Al, and 1.5 mm thick Cu filters are proven to reduce the dose inhomogeneity in RPL samples to about 30 %, 15 %, and 8 % respectively.

To improve dose homogeneity, the use of an appropriate thickness of Al filter is found to be suitable for the present study. The effect of different voltages has been evaluated as well, aiming at verifying the possible use of the irradiator at its maximum tension as well. With the shielding configuration, the absorbed dose of the RPL dosimeter at 160 kV X-ray tube voltage irradiation condition is slightly higher than at 100 kV tube voltage X-ray irradiation, due to an increase of the mean energy of the X-ray irradiator. The absorbed dose in silica for a relative comparison and water for a standard reference dosimeter is also studied in Monte Carlo simulations.

Additionally, as a relevant outcome of this work, a calibration factor is calculated to convert dose in water, typically provided by standard calibration systems, and the average dose absorbed by RPL dosimeters. With the use of a 1.5 mm Al thickness, this factor is found to be 3.7 in the selected irradiation conditions. This calibration factor was experimentally validated by an irradiation campaign of RPL dosimeters performed in the frame of a parallel study, realized in collaboration with CERN. The satisfactory agreement with measurements validates the developed simulation system and the performed dosimetry calculations and contribute to provide dose values for the RPL dosimeters irradiated in the frame of other experimental activities.

Finally, the simulations and the experiments here reported confirm the possibility to use a commercial X-ray irradiator at a tension of 100 kV or 160 kV for the irradiation of various macroscopic samples of RPL dosimeter, water and silica having a thickness up to at least 1.5 mm, being much thicker that the samples normally irradiated in this facility, mostly optical fibers. Satisfactory dose homogeneity is achieved by hardening the produced X-ray spectrum with the use of simple layers of 1.5 mm of Al.

This approach and the collected satisfactory results pave the way for uses of commercial X-ray facilities for the irradiation of various materials and samples, for a variety of scientific activities, ranging from dosimetry to the characterization of radiation-tolerant devices and integrated systems. A wide range of applications, including but not limited to space, accelerators, nuclear sector, management of radioactive waste, medical physics will benefit from this possible use of X-ray facilities.

4.2 Future Works

For future studies, the used calibration factor, whose validity as present is limited to the investigated set of irradiation conditions, has to be determined for higher X-ray tube voltages and different kinds of irradiation conditions including filters such as copper, lead, and tungsten.

PHITS simulations were found to be underestimating the characteristics X-ray spectrum in comparison to SpekPy. This may be due to the approximations done in the realisation of the model. The anode thickness and specific geometry may have an impact on the production of X-ray photons and this has to be studied to be confirmed. Future refinements of the simulations will be realized, in which this model will be updated to look more like the actual facility configuration, and in which normalization factors will be determined to compare quantitatively the simulations with real photon fluences, which can be measured by spectroscopic techniques.

Chapter 5

References

[1] A. J. J. Bos, "Fundamentals of radiation dosimetry," in *AIP Conference Proceedings*, 2011, pp. 5–23. doi: 10.1063/1.3576156.

[2] E. B. Podgorsak, *Radiation Physics for Medical Physicists*. Springer Science & Business Media, 3rd ed., 2016. [Online]. DOI: 10.1007/978-3-319-25382-4.

[3] J. Harb *et al.*, "Femtosecond Direct Laser Writing of Silver Clusters in Phosphate Glasses for X-ray Spatially-Resolved Dosimetry," *Chemo sensors*, vol. 10, no. 3, Mar. 2022, doi: 10.3390/chemosensors10030110.

[4] M. A. Maqbool, *An introduction to medical physics*. Cham, Switzerland: Springer, 2017. [Online]. DOI: 10.1007/978-3-319-61540-0.

[5] J. H. Hubbell, "Photon Mass Attenuation and Mass Energy-Absorption Coefficients for H, C, N, 0, Ar, and Seven Mixtures from 0.1 keV to 20 MeV*," 1977. [Online]. DOI: https://doi.org/10.2307/3574732

[6] Frank Herbert Attix, *Introduction to Radiological Physics and Radiation Dosimetry*. John Wiley & Sons, 2008. [Online]. DOI:10.1002/9783527617135

[7] S. García-Pareja, A. M. Lallena, and F. Salvat, "Variance-Reduction Methods for Monte Carlo Simulation of Radiation Transport," *Frontiers in Physics*, vol. 9, Oct. 2021, doi: https://doi.org/10.3389/fphy.2021.718873.

[8] PHITS User Guidelines, PHITS Homepage (jaea.go.jp) PHITS Website https://phits.jaea.go.jp/index.html. Accessed on: 04.08.2023

[9] A. Meyer, D. Lambert, A. Morana, P. Paillet, A. Boukenter, and S. Girard, "Simulation and Optimization of Optical Fiber Irradiation with X-rays at Different Energies," *Radiation*, vol. 3, no. 1, pp. 58–74, Mar. 2023, doi: 10.3390/radiation3010006.

[10] H. Seo, W. Kim, B. Han, H. Jang, M. S. Yoon, and Y. Lee, "Usefulness of an Additional Filter Created Using 3D Printing for Whole-Body X-ray Imaging with a Long-Length Detector," *Sensors*, vol. 22, no. 11, Jun. 2022, doi: 10.3390/s22114299

[11] G. Poludniowski, A. Omar, R. Bujila, and P. Andreo, "Technical Note: SpekPy v2.0—a software toolkit for modeling x-ray tube spectra," *Med Phys*, vol. 48, no. 7, pp. 3630–3637, Jul. 2021, doi: 10.1002/mp.14945.

[12] K. Niita *et al.*, " JAEA-Data/Code 2010-022 PHITS: Particle and Heavy Ion Transport code System, Version 2.23."

[13] L. Sihver *et al.*, "An update about recent developments of the PHITS code," *Advances in Space Research*, vol. 45, no. 7, pp. 892–899, Apr. 2010, doi: 10.1016/j.asr.2010.01.002.

[14] K. Niita, T. Sato, H. Iwase, H. Nose, H. Nakashima, and L. Sihver, "PHITS-a particle and heavy ion transport code system," *Radiat Meas*, vol. 41, no. 9–10, pp. 1080–1090, Oct. 2006, doi: 10.1016/j.radmeas.2006.07.013.

[15] Y. Iwamoto *et al.*, "Benchmark study of the recent version of the PHITS code," *J Nucl Sci Technol*, vol. 54, no. 5, pp. 617–635, May 2017, doi: 10.1080/00223131.2017.1297742.

[16] M. Z. Abdul Aziz *et al.*, "Monte Carlo simulation of X-ray room shielding in diagnostic radiology using PHITS code," *J Radiat Res Appl Sci*, vol. 13, no. 1, pp. 704–713, Jan. 2020, doi: 10.1080/16878507.2020.1828020.

[17] T. Sato, L. Sihver, H. Iwase, H. Nakashima, and K. Niita, "Simulations of an accelerator-based shielding experiment using the particle and heavy-ion transport code system PHITS," *Advances in Space Research*, vol. 35, no. 2, pp. 208–213, 2005, doi: 10.1016/j.asr.2005.01.041.

[18] T. Sato, K. Niita, H. Iwase, H. Nakashima, Y. Yamaguchi, and L. Sihver, "Applicability of particle and heavy ion transport code PHITS to the shielding design of spacecrafts," *Radiat Meas*, vol. 41, no. 9–10, pp. 1142–1146, Oct. 2006, doi: 10.1016/j.radmeas.2006.07.014.

[19] T. Furuta and T. Sato, "Medical application of particle and heavy ion transport code system PHITS," *Radiological Physics and Technology*, vol. 14, no. 3. Springer, pp. 215–225, Sep. 01, 2021. doi: 10.1007/s12194-021-00628-0.

[20] L. M. Carter *et al.*, "PARaDIM: A PHITS-Based monte carlo tool for internal dosimetry with tetrahedral mesh computational phantoms," *Journal of Nuclear Medicine*, vol. 60, no. 12, pp. 1802–1811, 2019, doi: 10.2967/jnumed.119.229013.

[21] T. Sato *et al.*, "Features of Particle and Heavy Ion Transport code System (PHITS) version 3.02," *J Nucl Sci Technol*, vol. 55, no. 6, pp. 684–690, Jun. 2018, doi: 10.1080/00223131.2017.1419890

[22] A. Mesbahi and S. S. Zakariaee, "Effect of anode angle on photon beam spectra and depth dose characteristics for X-RAD320 orthovoltage unit," *Reports of Practical Oncology and Radiotherapy*, vol. 18, no. 3, pp. 148–152, 2013, doi: 10.1016/j.rpor.2012.12.001.

[23] Mohammad Reza Ay, M. Shahriari, S. Sarkar, M. Adib, and H. Zaidi, "Monte Carlo simulation of x-ray spectra in diagnostic radiology and mammography using MCNP4C," *Physics in Medicine and Biology*, vol. 49, no. 21, pp. 4897–4917, Nov. 2004, doi: https://doi.org/10.1088/0031-9155/49/21/004

[24] Comet MXR -165 X-ray Irradiator Specification, https://x-ray.comet.tech. Accessed on: 10 August ,2023

[25] D. Pramberger, Y. Q. Aguiar, J. Trummer, and H. Vincke, "Characterization of Radio-Photo-Luminescence (RPL) Dosimeters as Radiation Monitors in the CERN Accelerator Complex," *IEEE Trans Nucl Sci*, vol. 69, no. 7, pp. 1618–1624, Jul. 2022, doi: 10.1109/TNS.2022.3174784.

[26] K. Hiramatsu, S. Yoshihashi, S. Kusaka, F. Sato, E. Hoashi, and I. Murata, "Gamma-Ray Dose Measurement with Radio-Photoluminescence Glass Dosimeter in Mixed Radiation Field for BNCT."

[27] T. Yamamoto, A. Rosenfeld, T. Kron, F. d'Errico, and M. Moscovitch, "RPL Dosimetry: Principles and Applications," AIP, Jul. 2011, pp. 217–230. doi: 10.1063/1.3576169.

[28] Ž. Knežević, L. Stolarczyk, I. Bessieres, J. M. Bordy, S. Miljanić, and P. Olko, "Photon dosimetry methods outside the target volume in radiation therapy: Optically stimulated luminescence (OSL), thermoluminescence (TL) and radiophotoluminescence (RPL) dosimetry," *Radiat Meas*, vol. 57, pp. 9–18, 2013, doi: 10.1016/j.radmeas.2013.03.004.

[29] T. Kurobori, "Performance characterisation of a real-time fiber dosimetry system using radiophotoluminescent glasses," *Jpn J Appl Phys*, vol. 57, no. 10, Oct. 2018, doi: 10.7567/JJAP.57.106402.

[30] Thompson, A.; Attwood, D.; Gullikson, E.; Howells, M.; Kim, K.J.; Kirz,J.; Kortright, J.; Lindau, I.; Pianetta, P.; Robinson, A. X-ray Data Booklet; Lawrence Berkeley National

Laboratory: Berkeley, CA, USA, 2009. Available online: https://xdb.lbl.gov (accessed on 03 July, 2023).

[31] K. H. Chadwick and W. F. Oosterheert, "Dosimetry concepts and measurements in food irradiation processing," *International Journal of Radiation Applications and Instrumentation. Part A. Applied Radiation and Isotopes*, vol. 37, no. 1, pp. 47–52, Jan. 1986, doi:https://doi.org/10.1016/0883-2889(86)90195-4.

[32] F. Stichelbaut *et al.*, "The Palletron™: a high-dose uniformity pallet irradiator with X-rays," *Radiation Physics and Chemistry*, vol. 71, no. 1–2, pp. 291–295, Sep. 2004, doi: https://doi.org/10.1016/j.radphyschem.2004.03.062.

[33] M. Ferrari et al., "Characterization of Radio-Photo-Luminescence dosimeters under X-ray irradiation", IEEE TRANSACTIONS ON NUCLEAR SCIENCE, VOL. XX, NO. XX, XXXX 2023, accepted to RADECS 2023 and in preparation.

[34] Dosimetry Solutions for Radiation Medicine https://www.ptwdosimetry.com/en/. Accessed on: 10 August, 2023